

THIS PAGE IS UNCLASSIFIED

ERRATA

NACA Research Memorandum L57K29

By William M. Bland, Jr., Andrew G. Swanson,
and Ronald Kolenkiewicz
January 1958

Page 21: In table I, change the last number in column 4 under the heading "Motor weight, lb" from 40 to 46.

Pages 33 and 34: In figures 9(a) and 9(b), change the multiplication factor at the top of the ordinate scale for R_{∞}/ft from $\times 10^3$ to $\times 10^6$.

Issued 5-14-58

NACA - Langley Field, Va.

THIS PAGE IS UNCLASSIFIED

NATIONAL ADVISORY COMMITTEE FOR AERONAUTICS

RESEARCH MEMORANDUM

FREE-FLIGHT AERODYNAMIC-HEATING DATA AT MACH NUMBERS

UP TO 10.9 ON A FLAT-FACED CYLINDER

By William M. Bland, Jr., Andrew G. Swanson,
and Ronald Kolenkiewicz

SUMMARY

A five-stage rocket-propelled model has been flown up to a Mach number of 10.9 and a corresponding free-stream Reynolds number of 6.57×10^6 , based upon nose diameter. Maximum Mach number was attained at an altitude of 49,300 feet as the model flew along a reentry-type trajectory at nearly zero angle of attack. Temperatures were measured at 16 stations on the inside of a flat-faced cylinder made of copper. Maximum temperatures of $1,085^\circ \text{F}$ and 820°F were measured inside the flat face and the cylindrical sides, respectively, at the end of the test. Aerodynamic-heating rates, derived from the temperature measurements and corrected for conduction effects, reached a maximum value of about 495 Btu/(sec)(sq ft) on the flat face (near the corner) and less than 170 Btu/(sec)(sq ft) on the cylindrical sides.

Experimental aerodynamic-heating rates near the center of the flat face, though generally lower, varied about the same as that predicted by a theory for equilibrium-dissociated laminar flow as the Mach number increased. The experimental heating rates increased as the corner was approached with the rate at the temperature measuring station nearest the corner for which heat-transfer data could be obtained being almost $1\frac{1}{2}$ times the rate near the center of the flat face. On the cylindrical sides of the nose, well downstream of the corner, the heating rates were low and appeared to agree fairly well with theoretical values for laminar flow.

INTRODUCTION

The problems associated with aerodynamic heating of bodies moving at supersonic and hypersonic speeds are currently being investigated by the Langley Pilotless Aircraft Research Division by means of techniques that utilize rocket-propelled models in free flight. Results of some



recent flight tests during which aerodynamic heating was measured on the noses of fairly slender bodies of revolution are reported in reference 1 at Mach numbers up to 10.4, in reference 2 at Mach numbers up to 9.89, and in reference 3 at Mach numbers up to 15.5. Other flight tests have been conducted to investigate anticipated benefits of nose blunting (as discussed in ref. 4) in reducing the aerodynamic heat transferred to noses. Results of some of these tests are presented in reference 5 at Mach numbers up to 14.6 and in reference 6 at Mach numbers up to 6.7. A perfectly flat nose (flat-faced cylinder), which is an extreme case of blunting, was tested as reported in reference 7 up to a maximum Mach number of 13.9 at an altitude of 81,500 feet where the free-stream Reynolds number was 1.60×10^6 , based upon the nose diameter.

The present report presents results of a flight test of another model with a flat nose of similar size and construction as that of reference 7. The test was made with the same five-stage rocket system used for the tests of references 3, 5, and 7, but was made along a reentry-type trajectory that resulted in lower altitudes at the time of maximum Mach number. This trajectory resulted in a maximum Mach number of 10.9 at an altitude of 49,300 feet where the free-stream Reynolds number was 6.57×10^6 , based upon nose diameter.

The flight test was conducted at the Langley Pilotless Aircraft Research Station at Wallops Island, Va., on June 19, 1957. The fourth-stage rocket motor (JATO, 1.52-KS-33,550, XM19 "Recruit") used in this investigation was made available by the U. S. Air Force.

SYMBOLS

A_{n+1}	cross-sectional area between elements n and $n + 1$, sq ft unless otherwise specified
A_{n-1}	cross-sectional area between elements n and $n - 1$, sq ft unless otherwise specified
A_p	cross-sectional area of pipe support, sq ft
a_0	speed of sound at stagnation point, ft/sec
c	specific heat, Btu/slug- $^{\circ}$ R
g	acceleration due to gravity, 32.2 ft/sec 2
h	enthalpy, $\frac{cT}{g} + \frac{V^2}{2gJ}$, Btu/lb



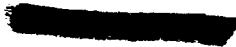
J	mechanical equivalent of heat, 778 ft-lb/Btu
k	thermal conductivity, Btu/(ft)(sec)(°R)
l_{n+1}	distance between thermocouple locations of elements n and n + 1, ft unless otherwise specified
l_{n-1}	distance between thermocouple locations of elements n and n - 1, ft unless otherwise specified
l_{13-14}	distance between thermocouples 13 and 14, ft
l_{13}	distance from forward end of pipe support to thermocouple 13, ft
M	Mach number
N_{Le}	Lewis number
$\bar{N}Nu$	Nusselt number
N_{St}	Stanton number
N_{Pr}	Prandtl number
q	heating rate, Btu/(sec)(sq ft)
Δq	change in q due to heat losses through pipe support, Btu/(sec)(sq ft)
r_n	radial length to thermocouple n, ft
$r_{m,p}$	mean radius of pipe support, ft
R	nose radius, 0.2135 ft (2.5625 in.)
Re_∞	Reynolds number based on free-stream conditions
Re_θ	Reynolds number based on local conditions and momentum thickness
S_n	surface area exposed to airstream of element n, sq ft unless otherwise specified
t	time, sec

CONFIDENTIAL

T	temperature, °R or °F
V	velocity, ft/sec
V _C	ambient acoustic velocity, ft/sec
x	distance along surface of nose starting at stagnation point, ft
$\left(\frac{du}{dx}\right)_o$	velocity gradient at stagnation point, 1/sec
θ	boundary-layer momentum thickness, ft
ρ	density, slugs/cu ft
τ	thickness, ft

Subscripts and abbreviations:

a	aerodynamic heating (data corrected for lateral heat flow)
n	element or thermocouple number
o	local flow conditions at stagnation point
p	pipe support
s	local flow conditions at stagnation point based on wall temperature
t	stagnation point
t,th	theoretical stagnation point
T.C.	thermocouple
w	wall or skin
1-D	one dimensional
∞	free stream



MODEL, INSTRUMENTATION, AND TEST TECHNIQUE

Model

The model, as shown in figure 1, was a body of revolution 63.50 inches long having a flat nose, a stepped cylindrical midsection, and a conical frustum with a total angle of 20° at the tail.

The 5.125-inch-diameter nose, shown in detail in figure 2, was machined from electrolytic copper. The nose was nominally 0.200 inch thick along the flat face and 0.133 inch thick along the cylindrical sides. Inside the nose was a steel radiation shield that protected the instruments and telemetering equipment from radiation from the hot nose walls. The shield joined the rear of the nose through an insulating Micarta support. A short steel pipe projected forward from the front of the radiation shield to provide additional support for the front face of the nose when the copper became hot. At ambient sea-level conditions, the pipe did not touch the inside surface of the front face, but was separated from this surface by a 0.020-inch-wide air gap. Late in the test, when the front face became hot and deflected slightly under the airload, it touched the pipe which gave additional support to prevent further deflection.

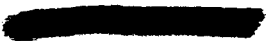
The forward cylindrical midsection of double-wall construction housed most of the telemetering equipment. A short conical frustum, having a total angle of 20° , connected the forward cylindrical section with the larger rear section which contained the fifth-stage rocket motor.

Stabilization of the model was achieved by a conical frustum having a total angle of 20° attached to the rear of the model. In addition to stabilizing the model, the frustum also served as an extension to the rocket-motor nozzle.

All external surfaces of the model were polished. Measurements indicated an average surface roughness of about 70 microinches across the flat face and about 40 microinches along the cylindrical surfaces of the test nose. Photographs of the nose and of the complete model are presented in figures 3 and 4, respectively.

Instrumentation

Measurements by 18 thermocouples and 4 accelerometers were transmitted during the flight test by a six-channel telemeter. The thermocouples were made of no. 30 gage chromel and alumel wires which were beaded together into balls that were peened into small holes in the inner surface of the



copper nose at the positions indicated in figure 2. Distances from the stagnation point to each thermocouple and the wall thickness measured at each thermocouple station are also presented in figure 2.

Three constant voltages and the outputs of each of six thermocouples were commutated and transmitted on one telemeter channel at rates of about 6 times per second and 12 times per second, respectively. On another telemeter channel, three constant voltages and the outputs of 12 thermocouples were commutated and transmitted at rates of about 6 times per second. The constant voltages were chosen to be equivalent to the lowest, middle, and highest temperatures anticipated in order to serve as an inflight calibration of the thermocouple-telemeter systems.

Each of the remaining four telemeter channels was used to transmit continuous measurements of one of four accelerometers; two measured longitudinal acceleration, one measured transverse acceleration, and one measured normal acceleration. These accelerometers were calibrated in standard earth gravitational units for the following ranges in which the positive values indicate thrust or positive force acting on the model:

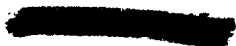
One longitudinal accelerometer, g units	-25 to 140
One longitudinal accelerometer, g units	-100 to 140
Transverse and normal accelerometers, g units	-25 to 25

Other instrumentation consisted of ground-based radar units for measuring model velocity and for obtaining the position of the model in space. The velocity measuring unit tracked the model for the first 30 seconds of the flight. For times thereafter, velocity was obtained by differentiating range data and integrating the longitudinal-accelerator measurements. Atmospheric conditions and wind data were measured to an altitude of 103,000 feet by a rawinsonde carried aloft by a balloon which was tracked by a modified radar unit. These measurements were made at the altitude of the hypersonic portion of the flight within approximately 30 minutes of the flight.

Test Technique

The desired performance was attained by using a five-stage propulsion system consisting of solid-fuel rocket motors. The model, which contained one of the rocket motors, and the four booster stages are shown in figure 5 as they appeared just after take-off from the launcher. Characteristics of the rocket motors employed during the flight test are presented in table I.

The model-booster combination was launched at an angle of 73° above the horizontal. The first two stages, in delayed sequence, were used to



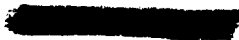
propel the remaining stages along a ballistic trajectory that reached a peak altitude of approximately 92,500 feet. Coasting flight continued after peak altitude until a preset timer ignited the third-stage rocket motor at 97.04 seconds. At this time, the flight-path angle was 33° below the horizontal. After the third-stage rocket motor burned out, the model and attached booster stages coasted for about $6\frac{1}{2}$ seconds so that the maximum velocity portion of the flight test would occur at low altitudes. The last two stages were fired in rapid sequence to accelerate the model to the maximum Mach number at an altitude of 49,300 feet.

DATA REDUCTION

The aerodynamic-heating rate at each temperature measuring station was obtained by first making a one-dimensional thick-wall analysis with the method of reference 8. For the present analysis, a constant value of wall specific heat was assumed, the value used being that for a temperature midway between the highest and lowest measured temperatures for each station. (The use of a constant specific heat should introduce small error in the data.) Time histories of the inside wall temperatures (obtained from faired curves through the measured data points) were used to compute time histories of the outside wall temperatures. These computed outside wall temperatures were then used to determine a heat input to the wall. Values of the heating rate thus obtained by the one-dimensional analysis were further corrected for the lateral heat flow caused by the temperature gradients along the skin and for heat flow into a pipe support behind the flat face to give the aerodynamic-heating rates. Radiation losses have been estimated to be negligible and have, therefore, been neglected.

This method of data reduction assumes that the lateral and pipe-support heat flows do not affect the temperature gradient through the skin (that is, that the independent heat flows calculated can be superimposed). Except near the corner, this assumption is believed to be reasonably valid and to introduce negligible error. Corner effects are discussed subsequently.

Calculations of the lateral-heating-rate values were carried out in a manner similar to that applied in reference 7, that is, the nose was divided into annular elements, one for each thermocouple position, and it was assumed that the temperature of each element was that of the included thermocouple. The following relation was used to calculate the aerodynamic-heating rate to any element n except for elements 2 and 3 where additional corrections were needed:



$$q_a = q_{1-D} + \frac{kA_{n+1}}{S_n} \frac{T_n - T_{n+1}}{l_{n+1}} + \frac{kA_{n-1}}{S_n} \frac{T_n - T_{n-1}}{l_{n-1}} \quad (1)$$

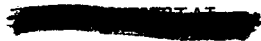
Evaluation of A_{n-1} , A_{n+1} , S_n , l_{n-1} , and l_{n+1} is straightforward except in the region of the corner. Here the presence of severe lateral temperature gradients and question as to the validity of the one-dimensional analysis make rather dubious the superposition of the independent heat-flow calculations. Combined with a marked sensitivity of lateral-heat-flow corrections to relatively small changes in assumed block arrangements, this renders great uncertainty to results obtained in the corner by this method. For completeness, however, A , S , and l for one assumed block arrangement are presented for all stations in the following table, and these values were used to obtain the results presented in this report:

n	A_{n-1} , sq in.	A_{n+1} , sq in.	S_n , sq in.	l_{n-1} , in.	l_{n+1} , in.
1	0.314	0.314	0.196	0.625	0.375
2	.314	.942	1.571	.375	.500
3	.942	1.571	3.142	.500	.500
4	1.571	2.262	5.270	.500	.600
5	2.262	2.796	5.374	.600	.250
6	2.796	3.860	5.076	.250	.350
7	3.860	2.086	10.868	.350	.250
8	2.086	2.086	4.830	.250	.350
9	2.086	2.086	7.648	.350	.600
10	2.086	2.086	12.881	.600	1.000
11	2.086	2.086	20.528	1.000	1.550

The temperatures forming the forcing functions for the lateral-heat-flow terms in equation (1) were assumed to be the mean temperatures through the wall as expressed by

$$T_{\text{mean}} = T_{\text{inside}} + \frac{T_{\text{outside}} - T_{\text{inside}}}{3} \quad (2)$$

Equation (2) is exact for a ramp-type heat input.



Other corrections to the heating rates at temperature measuring stations 2 and 3 were necessary to account for heat flow into the pipe support whenever the front face deflected enough to touch the pipe. This flow was accounted for by the following equations:

$$\Delta q_2 = \left[\frac{(\rho c \tau)_p 2\pi r_{m,p}}{S_2} l_{13} \left(\frac{dT_w}{dt} \right)_{13} + \frac{k_p A_p}{l_{13-14}} \frac{T_{13} - T_{14}}{S_2} \right] C_2 \quad (3)$$

$$\Delta q_3 = \left[\frac{(\rho c \tau)_p 2\pi r_{m,p}}{S_3} l_{13} \left(\frac{dT_w}{dt} \right)_{13} + \frac{k_p A_p}{l_{13-14}} \frac{T_{13} - T_{14}}{S_3} \right] C_3 \quad (4)$$

where

$$C_2 = \frac{T_2}{T_2 + T_3}$$

and

$$C_3 = \frac{T_3}{T_2 + T_3}$$

The first term within the brackets of equations (3) and (4) represents the portion of the heat flow that raised the temperature of the pipe at the forward temperature measuring station, and the second term represents the heat flowing from the first to the second temperature measuring stations. The terms within the brackets are modified by C_2 and C_3 which proportion the quantity of heat supplied to the pipe by each block.

This method underestimates the heat flow into the pipe somewhat since it neglects some of the heat stored in the region between the front end of the pipe support and the forward thermocouple (because of the probable existence of higher temperatures at the forward end of the pipe than at the forward thermocouple). The amount of heat stored in this manner is expected to be small. A straight-line extrapolation of the temperatures at the two temperature measuring stations on the pipe to the forward end of the pipe support was also used to estimate the heat flow down the pipe. Results obtained were similar to the ones obtained by the present analysis. The maximum correction to the heating rates because of heat flow to the pipe was 4.4 percent at station 2 and 6.8 percent at station 3.

ACCURACY

The measured temperatures are believed to be accurate within ± 1 percent of the full-scale range of the thermocouples. Therefore, any temperature measurement is believed to be accurate to within $\pm 24^{\circ}$ F. Values of the one-dimensional heating rate are believed to be accurate to within ± 5 percent on the flat face and ± 15 percent on the cylindrical sides during periods of high heating rate. The accuracy of the calculated lateral-conduction heating-rate values is not known; however, at the temperature measuring stations where the conduction corrections are small, large errors in conduction heating rate would have a small effect on the magnitude of the aerodynamic-heating rate. For temperature measuring stations near the corner of the nose, the calculated lateral-conduction corrections were large and were subject to considerable variation in magnitude. There, changes in magnitude were dependent upon the particular physical parameters used in computing the lateral-conduction heating rate; thus, aerodynamic-heating rates for the corner region could be in considerable error and are not presented herein. The possible error in Mach number at the time of third-stage ignition is estimated to be about ± 0.1 . Because of the method used to obtain velocity after ignition of the third-stage rocket motor (integration of the longitudinal-accelerometer measurements), the possible error in Mach number accumulated to the end of the flight test. This error in Mach number amounted to about ± 0.7 between the time of ignition of the third-stage rocket motor and the end of the flight. Therefore, the Mach number at the end of the test is estimated to be accurate within ± 0.8 . In view of the consistency of velocity increments obtained from trajectory computations using estimated drag and rocket-motor performance with those obtained from comparable rocket motors of the model reported herein and those of references 3, 5, and 7, it is believed that the Mach numbers quoted in this report are more accurate than the aforementioned ± 0.8 .

RESULTS AND DISCUSSION

Flight Test

Flight-test data were obtained as the model went along the trajectory shown in figure 6. Times of significant events are indicated on the trajectory. Performance of the model and atmospheric conditions along the flight path as measured by the rawinsonde are presented as functions of time in figures 7, 8, and 9. A maximum Mach number of 10.9 was attained at an altitude of 49,300 feet as the model flew along a reentry-type trajectory that was inclined about 38° below the horizontal at the time of maximum Mach number. At the time of maximum Mach number the free-stream

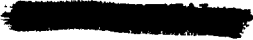
Reynolds number was 6.57×10^6 , based upon body diameter. The Reynolds number based upon the momentum thickness at the most outboard station on the flat face R_θ was 202. (The Reynolds number based upon the momentum thickness was calculated by the approximation $R_\theta = 0.664\sqrt{\tilde{R}}$ (ref. 9) where \tilde{R} is the integrated Reynolds number. The calculated pressure distribution for $M = 1.5$ from ref. 10 was used to calculate the integrated Reynolds number.)

Wall Temperatures

Time histories of measured inside wall temperatures at several measuring stations on the nose are presented in figure 10 for the time interval between 101.0 and 110.3 seconds. The curves presented are fairings through the measured data points. These data points were no more than $\pm 20^\circ$ R away from the faired curve (except for a few isolated points) and were generally less than $\pm 5^\circ$ R away from the faired curve. Temperatures picked off the faired data curves at each temperature measuring station are presented at 0.2-second intervals in table II. The measured wall temperatures increased rapidly at the end of the flight test to maximum values of $1,085^\circ$ F at temperature measuring station 5 ($x/R = 0.820$) on the flat nose and 820° F at temperature measuring station 7 on the cylinder. Maximum rates of temperature rise at these stations were 428° per second and 328° per second, respectively.

From 107.7 seconds to 108.8 seconds (most of the interval of fourth-stage rocket-motor firing), the temperatures were not commutated because of a temporary malfunction in the switching mechanism. Data presented for this interval were obtained by joining measured temperatures on either side of the interval with a faired curve. These fairings, through necessity, were somewhat arbitrary, but were tempered by making them vary in about the same manner as the temperature did at the temperature measuring station on which the switching mechanism stopped (temperature measuring station 1).

A computational method of reference 8 was used to calculate the temperature difference through the wall material so that the outside wall temperature, presented for several stations in figure 11, could be determined. Maximum temperature differences through the corner wall were found to be 55° R through the 0.200-inch-thick flat nose and 28° R through the 0.133-inch-thick copper on the cylindrical sides.



Heat-Transfer Data

Values of the heating rate have been computed by the one-dimensional analysis of reference 8 (as discussed in the "Data Reduction" section of this report) at each temperature measuring station except at those stations immediately adjacent to the corner (stations 6 and 7). The heat-flow mechanism in this region is believed to be too complex to be properly represented by the one-dimensional analysis. Time histories of the computed heating rates are presented in figure 12. Data points shown in this figure represent values that have been computed from the one-dimensional analysis. An idea of the accuracy of these heating rates can be obtained by comparing the data points with the curve faired through these points. Most of the data points agree with the faired curves within ± 5 Btu/(sec)(sq ft) which amounts to a difference, when the heating rates are highest, of about ± 2 percent on the flat portion of the nose and about ± 10 percent on the cylindrical portion. The distribution of the mean temperature across the flat nose and on the cylindrical sides is presented in figure 13 at selected times. From the temperature distribution, it is possible to observe by the magnitude of the temperature gradients that the conduction effects should be small at the earliest times for which data are presented, increase with Mach number (and time), and be largest in the region of the corner. These observations are borne out by the results presented in figure 12 which shows a comparison between the one-dimensional heating rates and aerodynamic-heating rates (the greater the difference between the curves the greater the lateral-conduction effects). The large effect and erratic behavior of the lateral conduction at station 8 probably result from incorrect mean temperatures at station 7 which stem from the inability of the one-dimensional analysis to cope with the heat flow in the region of the corner. Therefore, it is suggested that the aerodynamic-heating data presented for station 8 be treated as qualitative data.

During the times when the heating rates are high (after 108.8 seconds), the lateral-conduction corrections, except near the corner, are probably fairly accurate and any inaccuracies would probably not have significant effects on the overall picture. Before reaching 107 seconds, when the heating rates are low, the possible inaccuracies of the temperature measurements and the corrections lend sufficient uncertainties to make the aerodynamic-heating rates qualitative in nature.

Heat flow to the pipe support, which started after the front face made contact with the pipe at about 108.8 seconds, can be seen to have fairly small effect upon the aerodynamic-heating rates in figure 12. Contact between the front face, which was hot, and the pipe was signalled by an abrupt increase in the temperature of the forward end of the pipe.

~~CONFIDENTIAL~~

At the end of the test, the highest heating rate was found to be at temperature measuring station 5, which was located 0.82 of the distance from the stagnation point to the corner. However, this may not be the station of highest heating since the one-dimensional analysis supplied to the data was not considered applicable at station 6, which was located nearer the corner.

Measurement Repeatability and Effects of Angle of Attack

Some idea of the repeatability of the measurements and the effects of angle of attack can be obtained from the measured inside temperatures and one-dimensional heating rates presented in figures 14 and 15. In figure 14, temperature measurements and one-dimensional heating rates are presented for four temperature measuring stations on the flat nose equidistant from the center of the nose, but located 90° apart. Figure 15 contains temperature measurements and one-dimensional heating rates for two temperature measuring stations that were located the same axial distance behind the corner, but on opposite sides of the cylinder. In each of these figures the temperature measuring station marked "a" is located in the main line of thermocouples that starts near the center of the nose, crosses the flat nose, and extends along the cylinder.

In general, the measured wall temperatures and the one-dimensional heating rates at the four stations on the flat face show the same trends and levels. The temperature at station c is shown to be higher than the temperature at the other stations during the last part of the test, but only during the interval when the temperatures were not measured ($t = 107.7$ seconds to $t = 108.8$ seconds) do the faired curves differ enough to approach the magnitude of the quoted possible error. The one-dimensional heating rates on the flat nose are in fairly good agreement with one another. At the end of the test, differences between heating rates were of the order of the estimated accuracy.

On the cylinder, the measured temperatures and heating rates throughout most of the test were highest at temperature measuring station b. The differences noted in temperatures were about twice the size of the estimated possible errors.

From this discussion, it appears that effects, if any, of angle of attack on the heating of the front of the flat nose are submerged in the possible error of the measured temperatures and, thus, can be considered to be small. On the other hand, the differences observed in measured temperatures and one-dimensional heating rates at diametrically opposite temperature measuring stations on the cylinder are large enough to be studied in conjunction with the estimated angle of attack.

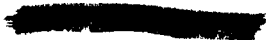
The angle of attack was not measured directly during the flight test; however, measurements made of accelerations along axes 90° apart in a plane normal to the longitudinal axis of the model made it possible to calculate the magnitude and direction of the force coefficient in a plane normal to the longitudinal axis. Results of these calculations combined with an estimated normal-force slope of 0.0709 per degree (as used in ref. 7), which is assumed to be linear at small angles of attack, indicate a trim angle of attack of about 1.1° with superimposed oscillations of about $\pm 0.9^\circ$. Thus, maximum angles of attack of about 2.0° are estimated to have occurred during the flight of the model (at times after 109.03 seconds). The angle of attack was zero for the earlier part of the flight test. During the time that the model was at an angle of attack, it was also apparently rolling in a random manner that resulted in placing the temperature measuring stations on the cylinder on the windward (high heating) side at various times for very short periods of time, thus making it impossible to say that the difference in temperature and one-dimensional heating rate was due to the estimated angle of attack.

A possible explanation for the difference in heating on the sides of the cylinder concerns the manner in which the flow reattaches downstream of the flat nose (around the corner); that is, an unsymmetrical reattachment pattern caused by an unsymmetrical nose or unsymmetrical flow (small angle of attack) could possibly cause differences in heating on the sides of the cylinder.

Comparison of Measured and Theoretical

Stagnation-Point Heating Rates

The aerodynamic-heating rates (one-dimensional heating rates corrected for lateral heat conduction) near the center of the flat face (temperature measuring station 1) are compared in figure 16 with theoretical stagnation-point heating rates predicted for laminar flow for a real gas by the method of reference 11, which assumes equilibrium dissociation in the boundary layer. The theoretical values were obtained by evaluating the expression

$$q = \frac{N_{Nu}}{\sqrt{R_s}} \frac{\sqrt{\rho_s \mu_s \left(\frac{du}{dx} \right)_0} (h_o - h_s)}{N_{Pr,s}}$$


where

$$\frac{N_{Nu}}{\sqrt{R_s}} = 0.67 \left(\frac{\rho_o \mu_o}{\rho_s \mu_s} \right)^{0.4}$$

for

$$N_{Le} = 1$$

and

$$N_{Pr} = 0.71$$

Parameters dependent upon wall temperature were evaluated at the outside wall temperature at temperature measuring station 1.

As in reference 7, the flow properties were obtained by applying the perfect gas relations of reference 12. Values of the viscosity of air were obtained from the Sutherland relation which has been shown, as discussed in reference 11, to make suitable predictions at temperatures below 16,200° R. The nondimensional rate of change of velocity at the stagnation point $\frac{R}{a_o} \left(\frac{du}{dx} \right)_o = 0.3$, as discussed in the appendix of reference 7, was obtained from a calculated pressure distribution for a Mach number of 1.5 (ref. 10). For the calculations in the present report, $\frac{R}{a_o} \left(\frac{du}{dx} \right)_o$ was assumed to be invariant with Mach number.

A comparison of experimental results with theoretical values in figure 16 shows good agreement through a large portion of the test. During the early part of the test (before 107 seconds) when the Mach numbers were relatively low and the aerodynamic heating was low, the somewhat erratic behavior of the experimental results was probably due to the uncertainties in the temperature measurements and in the conduction corrections. During the time of the test when the Mach number was high, the experimental heating rate increased about the same as that predicted by theory, but at a somewhat lower level. Differences between experiment and theory of about the same magnitude were also noted in reference 7.

RESEARCH REPORT

Measured and Theoretical Heating Rates
Over Front and Side of Nose

Variations of the ratio of local aerodynamic-heating rates to theoretical stagnation-point heating rates (ref. 11) with location on the nose are presented in figure 17 for several selected times. Before a time of 109 seconds, the variation across the flat face is irregular because of the previously mentioned uncertainties in the data, but after 109 seconds (when the heating rate was high) the local heating rate generally increased as the corner was approached. Also, the local heating rates inboard of station $x/R = 0.65$ were less than those predicted for the stagnation point by the theory of reference 11. The data presented include the effects of the pipe support on the two stations affected by this heat loss ($x/R = 0.195$ and $x/R = 0.390$). Reasonably large changes in heat loss to the support have little effect upon the magnitude of the data, thus indicating that the presence of the pipe support had little effect on the data.

Ratios of local heating rates to stagnation-point laminar heating rates have also been calculated by the methods of references 13 and 14 for conditions existing at $M = 1.5$ and by the calculated pressure distribution ($M = 1.5$) presented in reference 10. These ratios, included in figure 17(a), show an increase in heating rate as the corner is approached that is much the same as that exhibited by the experimental data at Mach numbers greater than 10.0.

It should be noted that the magnitudes of the ratios calculated by the methods in references 13 and 14 should not be compared with ratios made up of the experimental heating rates and the theoretical stagnation-point values computed by the method of reference 11. However, it is believed that the variations of these ratios across the flat face are comparable.

Since the aerodynamic-heating rate near the center of the flat face showed good agreement with values predicted by laminar theory (ref. 11) and the variation across the face was about the same as that predicted by other laminar theories (refs. 13 and 14), it seems reasonable to believe that the flow was laminar on the flat face; this was true at least as close to the corner as station $x/R = 0.82$ which was the most outboard position on the face for which aerodynamic heating was obtained. Thus, laminar flow was obtained for values of Re as high as 162 at a time when the ratio of wall temperature to total temperature (assuming that specific heat was constant) was about 0.1.

It can also be noted that, in general, the experimental heating rates on the face increased more rapidly than the predicted stagnation heating rate as the free-stream Reynolds number increased from 10.8×10^6

~~SECRET~~

($t = 109.0$ seconds) to 15.40×10^6 per foot ($t = 110.2$ seconds); whereas the Mach number remained relatively constant, and increased from 10.50 to only 10.92.

The variation with location of the ratio of local aerodynamic-heating rates to the theoretical stagnation-point heating rates (ref. 11) for temperature measuring stations along the cylinder (fig. 17(b)) is very irregular (even shows negative rates) near the corner. (The conduction-correction values here are admittedly inaccurate.) Downstream of the corner ($x/R > 1.4$), the heating rates become less erratic and, when compared with calculated heating rates based on laminar and turbulent flow, show better agreement with the values for laminar flow. Experimental values presented in figure 17(b) for the temperature measuring station at $x/R = 2.580$ do not include conduction corrections since no wall temperatures were measured downstream of this station. Conduction effects at this station should, however, be similar to those for the two stations immediately upstream: namely, small or negligible. Theoretical values on the cylindrical sides were calculated by using the laminar flat-plate theory of reference 15 and Van Driest's turbulent flat-plate theory as presented in reference 16 and modified by the Reynolds analogy relation

$$N_{St} = 0.6C_f$$

as suggested in reference 17. Local flow conditions were calculated by assuming that the pressure along the cylinder was equal to the free-stream ambient pressure and that the flow adjacent to the boundary layer had passed through a normal shock. The local viscosity was evaluated at the local temperature by the Sutherland relation; the recovery factors $N_{Pr}^{1/2}$ and $N_{Pr}^{1/3}$ for laminar and turbulent flow, respectively, were based upon the outside wall temperature; and the Reynolds number was based upon the distance from the stagnation point.

The values of the ratio of local one-dimensional heating rates to the one-dimensional heating rate at thermocouple 1 (near the nominal stagnation point) are presented in figure 18. The data are presented in this manner to show that, for this nose shape and for the conditions of the test, the heating was relatively uniform across the front face and the effect of conduction through and along the skin kept the heating rates at the corner relatively low instead of high as predicted by theory. This same effect is apparent in the temperature distribution presented in figure 13. Relieving effects of this nature could be of importance in the practical design of a missile nose.

CONCLUDING REMARKS

Temperature measurements have been made at 16 stations on the inside of a flat-faced cylinder that was tested on a rocket-propelled model up to a maximum Mach number of 10.9 at an altitude of 49,300 feet. The model flew along a reentry-type trajectory at nearly zero angle of attack during the high Mach number portion of the test.

Maximum temperatures of 1,085° F and 820° F were measured inside the flat face and the cylindrical sides, respectively, of the copper nose at the end of the test. Aerodynamic-heating rates derived from a one-dimensional analysis of the temperature measurements and corrected for lateral-conduction effects reached a maximum value of about 495 Btu/(sec)(sq ft) on the flat face (near the corner) and less than 170 Btu/(sec)(sq ft) on the cylindrical sides.

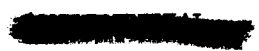
Experimental aerodynamic-heating rates near the center of the flat face, though generally lower, varied about the same as that predicted by a theory for equilibrium-dissociated laminar flow as the Mach number increased. Also, the variation of the experimental heating rates across the flat face was about the same as that predicted by theory at a Mach number of 1.5; that is, the heating rate at the temperature measuring station nearest the corner was almost $1\frac{1}{2}$ times the heating rate at the center of the flat face. On the cylindrical sides of the nose, well downstream of the corner, the heating rates were low and appeared to agree fairly well with theoretical values for laminar flow.

Langley Aeronautical Laboratory,
National Advisory Committee for Aeronautics,
Langley Field, Va., November 12, 1957.



REFERENCES

1. Bland, William M., Jr., and Collie, Katherine A.: Free-Flight Aerodynamic-Heating Data to Mach Number 10.4 for a Modified Von Kármán Nose Shape. NACA RM L56D25, 1956.
2. Bond, Aleck C., and Rumsey, Charles B.: Free-Flight Skin Temperature and Pressure Measurements on a Slightly Blunted 25° Cone-Cylinder-Flare Configuration to a Mach Number 9.89. NACA RM L57B18, 1957.
3. Bland, William M., Jr., Rumsey, Charles B., Lee, Dorothy B., and Kolenkiewicz, Ronald: Free-Flight Aerodynamic-Heating Data to a Mach Number of 15.5 on a Blunted Conical Nose With a Total Angle of 29°. NACA RM L57F28, 1957.
4. Allen, H. Julian, and Eggers, A. J., Jr.: A Study of the Motion and Aerodynamic Heating of Missiles Entering the Earth's Atmosphere at High Supersonic Speeds. NACA RM A53D28, 1953.
5. Rumsey, Charles B., and Lee, Dorothy B.: Heat-Transfer Measurements in Free Flight at Mach Numbers Up to 14.6 on a Flat-Faced Conical Nose With a Total Angle of 29°. NACA RM L57L03, 1957.
6. Garland, Benjamine J., Swanson, Andrew G., and Speegle, Katherine C.: Aerodynamic Heating and Boundary-Layer Transition on a 1/10-Power Nose Shape in Free Flight at Mach Numbers Up to 6.7 and Free-Stream Reynolds Numbers Up to 16×10^6 . NACA RM L57E14a, 1957.
7. Stoney, William E., Jr., and Swanson, Andrew G.: Heat Transfer Measured on a Flat-Face Cylinder in Free Flight at Mach Numbers Up to 13.9. NACA RM L57E13, 1957.
8. Hill, P. R.: A Method of Computing the Transient Temperature of Thick Walls From Arbitrary Variation of Adiabatic-Wall Temperature and Heat-Transfer Coefficient. NACA TN 4105, 1957.
9. Bromberg, Robert: A Note on the Calculation of Momentum Thickness Reynolds Number in a Boundary Layer With Pressure Gradient. Rep. No. GM-TN-21, the Ramo-Wooldridge Corp., Guided Missile Res. Div., May 11, 1956.
10. Maccoll, J. W., and Codd, J.: Theoretical Investigations of the Flow Around Various Bodies in the Sonic Region of Velocities. British Theoretical Res. Rep. No. 17/45, B.A.R.C. 45/19, Ministry of Supply, Armament Res. Dept., 1945.



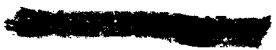
11. Fay, J. A., and Riddell, F. R.: Theory of Stagnation Point Heat Transfer in Dissociated Air. Res. Rep. 1, AVCO Res. Lab., June 1956 (rev. Apr. 1957). (Formerly AVCO Res. Note 18.)
 12. Ames Research Staff: Equations, Tables, and Charts for Compressible Flow. NACA Rep. 1135, 1953. (Supersedes NACA TN 1428.)
 13. Lees, Lester: Laminar Heat Transfer Over Blunt-Nosed Bodies at Hypersonic Flight Speeds. Jet Propulsion, vol. 26, no. 4, Apr. 1956, pp. 259-269.
 14. Stine, Howard A., and Wanlass, Kent: Theoretical and Experimental Investigation of Aerodynamic-Heating and Isothermal Heat-Transfer Parameters on a Hemispherical Nose With Laminar Boundary Layer at Supersonic Mach Numbers. NACA TN 3344, 1954.
 15. Van Driest, E. R.: Investigation of Laminar Boundary Layer in Compressible Fluids Using the Crocco Method. NACA TN 2597, 1952.
 16. Lee, Dorothy B., and Faget, Maxime A.: Charts Adapted From Van Driest's Turbulent Flat-Plate Theory for Determining Values of Turbulent Aerodynamic Friction and Heat-Transfer Coefficients. NACA TN 3811, 1956.
 17. Rubesin, Morris W.: A Modified Reynolds Analogy for the Compressible Turbulent Boundary Layer on a Flat Plate. NACA TN 2917, 1953.
- 

TABLE II
 PAIRED MEASURED TEMPERATURE VALUES

Time, sec	Temperature, °F, at station -																	
	1	2	3	4a	4b	4c	4d	5	6	7	8	9	10	11a	11b	12	13 (*)	14 (*)
101.0	183	183	193	185	188	179	188	188	180	178	171	169	168	164	159	163	86	90
101.2	186	185	194	187	189	183	189	190	183	180	174	171	168	165	160	163	86	90
101.4	190	188	195	190	191	186	190	192	185	182	176	172	168	166	161	164	86	90
101.6	194	192	197	193	194	189	193	195	188	185	178	173	168	167	161	165	86	90
101.8	197	196	199	196	196	193	195	197	190	188	180	175	169	167	161	166	86	90
102.0	200	200	202	200	200	197	198	200	193	190	183	177	170	168	162	167	86	90
102.2	204	204	205	204	204	200	201	204	196	192	185	178	171	169	163	168	86	90
102.4	207	208	209	208	207	204	205	207	198	195	187	180	171	170	163	168	86	90
102.6	211	212	213	211	210	208	208	210	202	197	189	181	171	171	164	169	86	90
102.8	215	215	215	215	214	212	212	214	204	199	191	183	172	171	165	170	86	90
103.0	218	219	219	219	218	215	215	217	207	203	193	185	172	172	166	171	86	90
103.2	221	223	223	223	221	218	219	221	210	205	195	186	173	173	167	172	86	90
103.4	225	226	227	227	225	221	223	225	212	207	198	187	174	174	168	172	86	90
103.6	229	230	230	230	229	225	226	228	215	210	200	189	175	175	170	173	86	90
103.8	232	233	235	234	233	229	230	233	217	213	203	191	177	175	171	174	86	90
104.0	235	237	237	238	236	232	234	237	220	215	205	192	178	176	172	175	86	90
104.2	240	240	242	242	240	235	237	240	223	217	207	194	180	177	173	176	86	90
104.4	244	245	247	245	244	239	241	244	226	220	209	195	182	178	175	177	86	90
104.6	248	249	249	249	247	243	245	248	228	223	212	197	183	179	176	177	86	90
104.8	252	254	253	253	251	246	248	252	231	225	214	199	185	179	177	178	86	90
105.0	256	257	256	256	254	249	253	255	234	228	216	200	187	181	179	179	86	90
105.2	260	260	260	260	258	253	255	259	237	230	218	202	188	181	180	180	86	90
105.4	265	265	265	264	262	257	259	263	240	233	221	203	190	182	181	181	86	90
105.6	269	269	269	268	266	260	264	268	243	235	223	205	192	183	182	182	86	90
105.8	273	271	273	272	270	264	268	272	245	237	225	206	193	184	183	183	86	90
106.0	275	275	277	274	274	268	272	276	248	240	227	208	195	184	184	183	86	90
106.2	279	278	280	278	278	270	275	279	251	243	229	210	197	185	185	184	86	90
106.4	282	282	284	281	282	273	277	283	245	235	213	198	186	187	185	185	86	90
106.6	285	285	286	283	285	275	280	285	257	247	235	214	200	187	188	185	86	90
106.8	287	286	287	285	288	277	284	288	261	249	239	216	202	188	190	186	86	90
107.0	290	288	288	287	291	279	286	289	265	251	242	217	204	189	192	188	87	90
107.2	293	292	292	290	294	283	288	292	270	253	245	219	206	190	193	190	87	90
107.4	299	299	298	295	302	290	295	294	278	254	247	221	208	191	196	193	87	90
107.6	310	308	309	304	313	301	304	298	286	257	250	224	211	193	198	196	87	90
107.8	325	325	326	316	326	316	315	313	297	263	254	226	214	195	202	200	87	90
(**)																		
108.0	346	344	346	332	341	339	330	337	313	269	257	230	218	198	205	204	87	90
108.2	378	367	370	355	362	369	354	368	332	276	255	234	224	204	111	210	87	91
108.4	394	393	401	389	389	407	388	404	357	297	264	238	232	211	223	217	88	91
108.6	427	427	438	431	428	453	430	450	392	321	289	248	239	220	239	226	88	92
108.8	467	467	483	482	480	507	481	499	441	358	285	263	249	234	259	237	91	99
109.0	515	515	534	543	545	569	542	557	503	413	317	282	262	252	285	251	94	123
109.2	568	567	593	610	618	638	611	624	568	469	356	304	278	273	313	270	97	180
109.4	628	628	657	682	690	709	683	696	640	528	398	327	299	295	340	291	107	245
109.6	694	693	724	757	764	783	757	773	714	590	439	354	323	318	367	311	124	315
109.8	764	759	798	833	838	856	832	853	793	652	483	384	348	341	395	333	146	384
110.0	837	835	874	909	914	932	908	935	837	714	527	417	373	364	423	354	170	454
110.2	915	917	954	987	992	1008	984	1020	953	777	571	450	400	387	453	376	196	525
Measured thickness, in. . . .	0.201	0.199	0.198	0.198	0.197	0.200	0.200	0.197	0.196	0.133	0.133	0.132	0.131	0.130	0.129	0.129	---	---

*Temperatures on pipe support.
 **Temperature not measured during this interval, except at station 1.

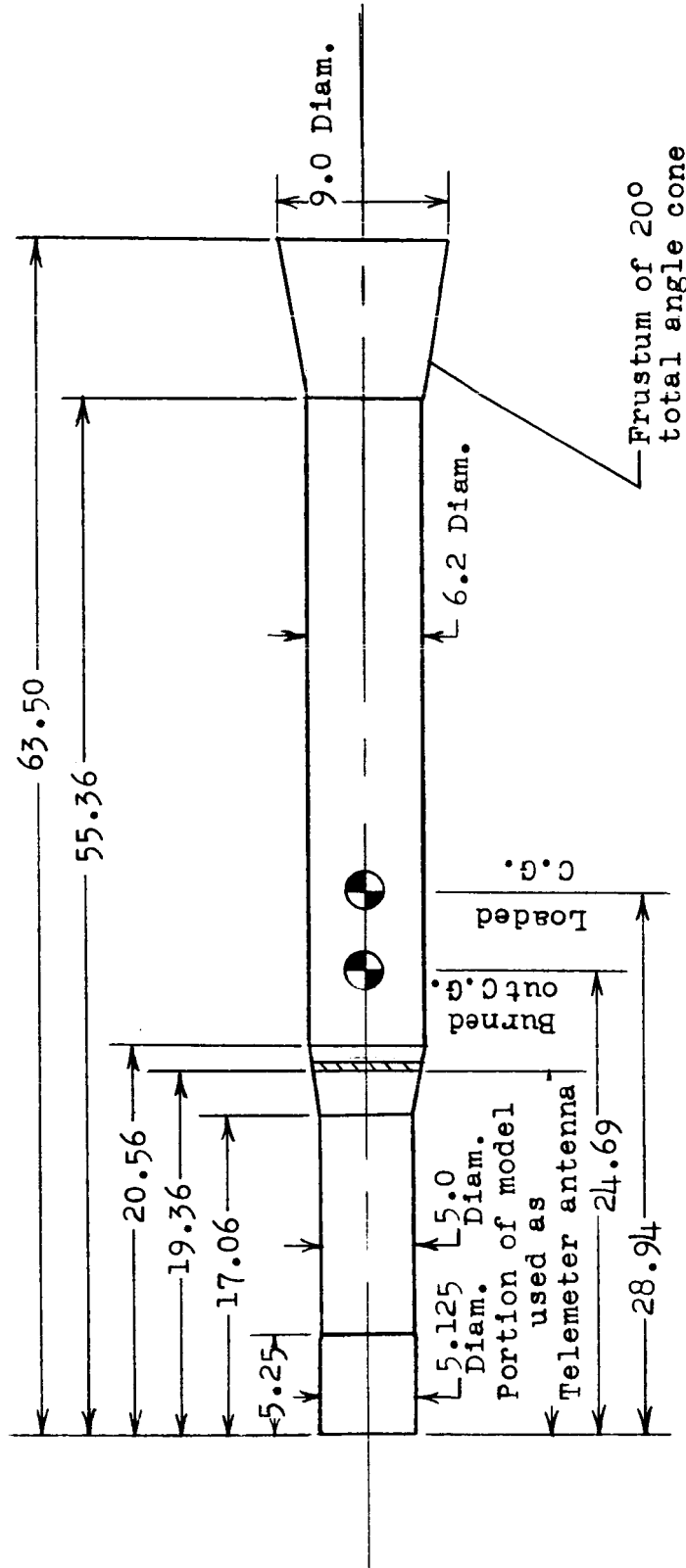


Figure 1.- Sketch of model (fifth stage). All dimensions are in inches.

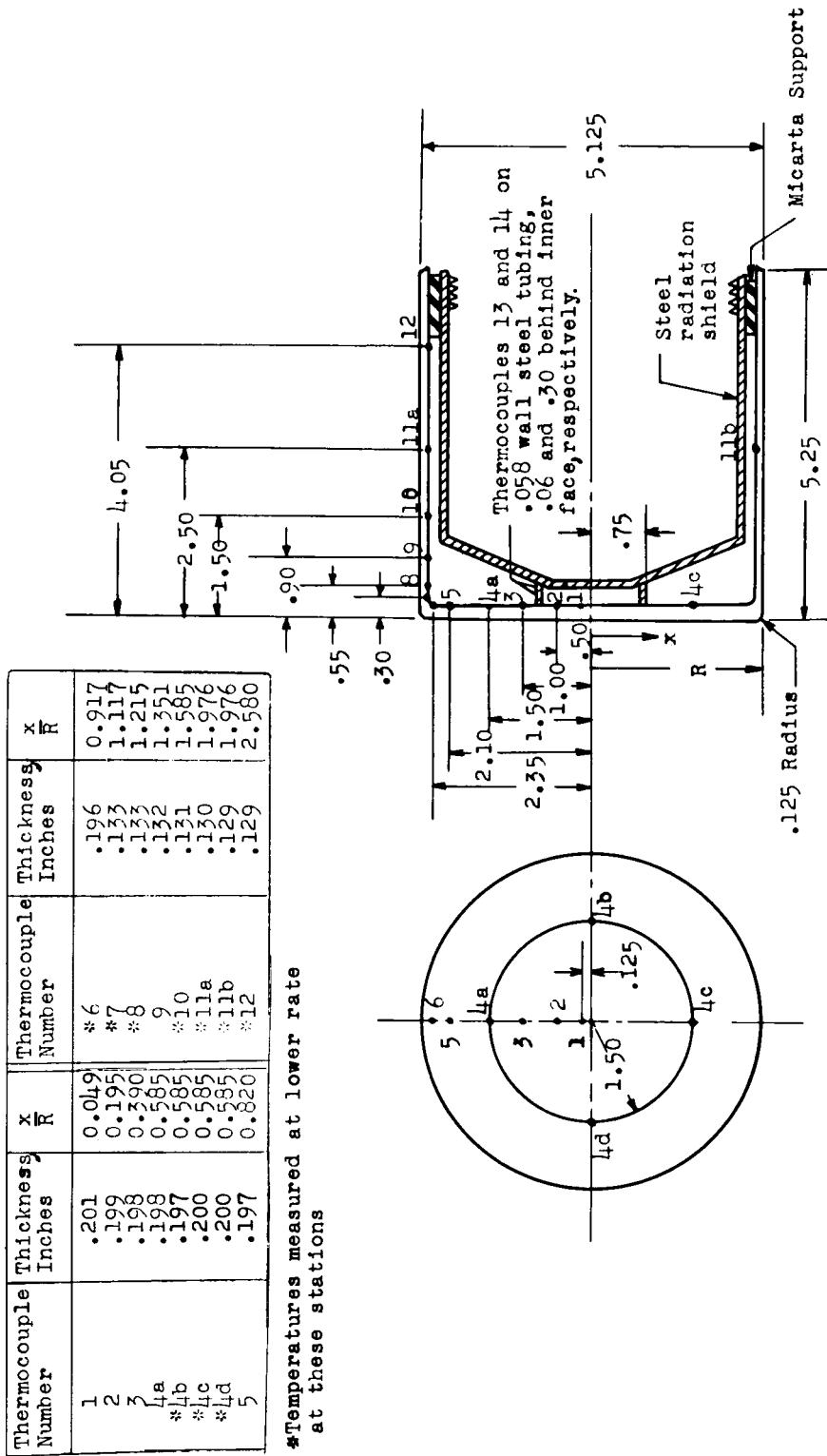


Figure 2.- Sketch of nose showing temperature measuring stations. All dimensions are in inches.

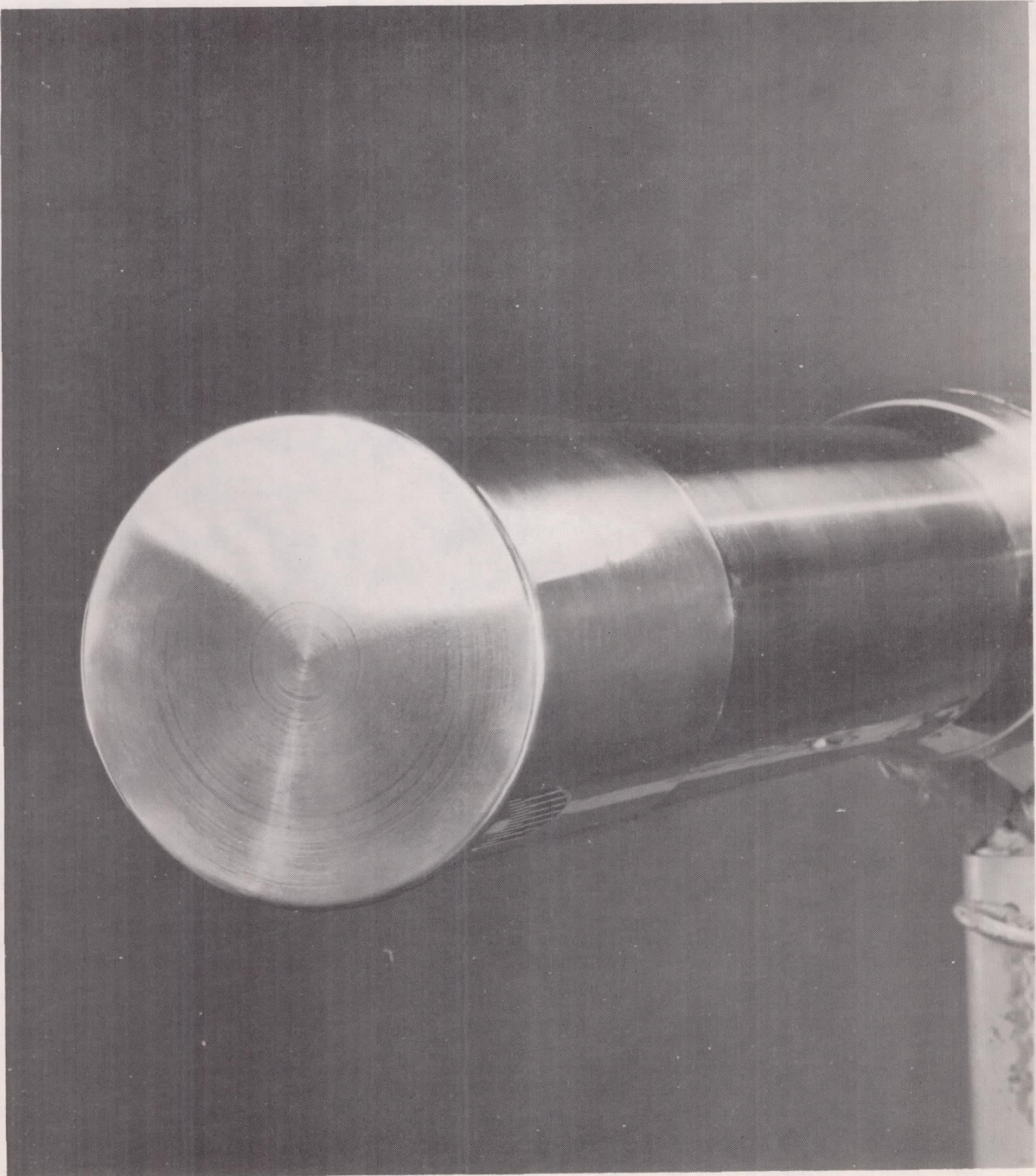


Figure 3.- Photograph of nose.

L-57-2395

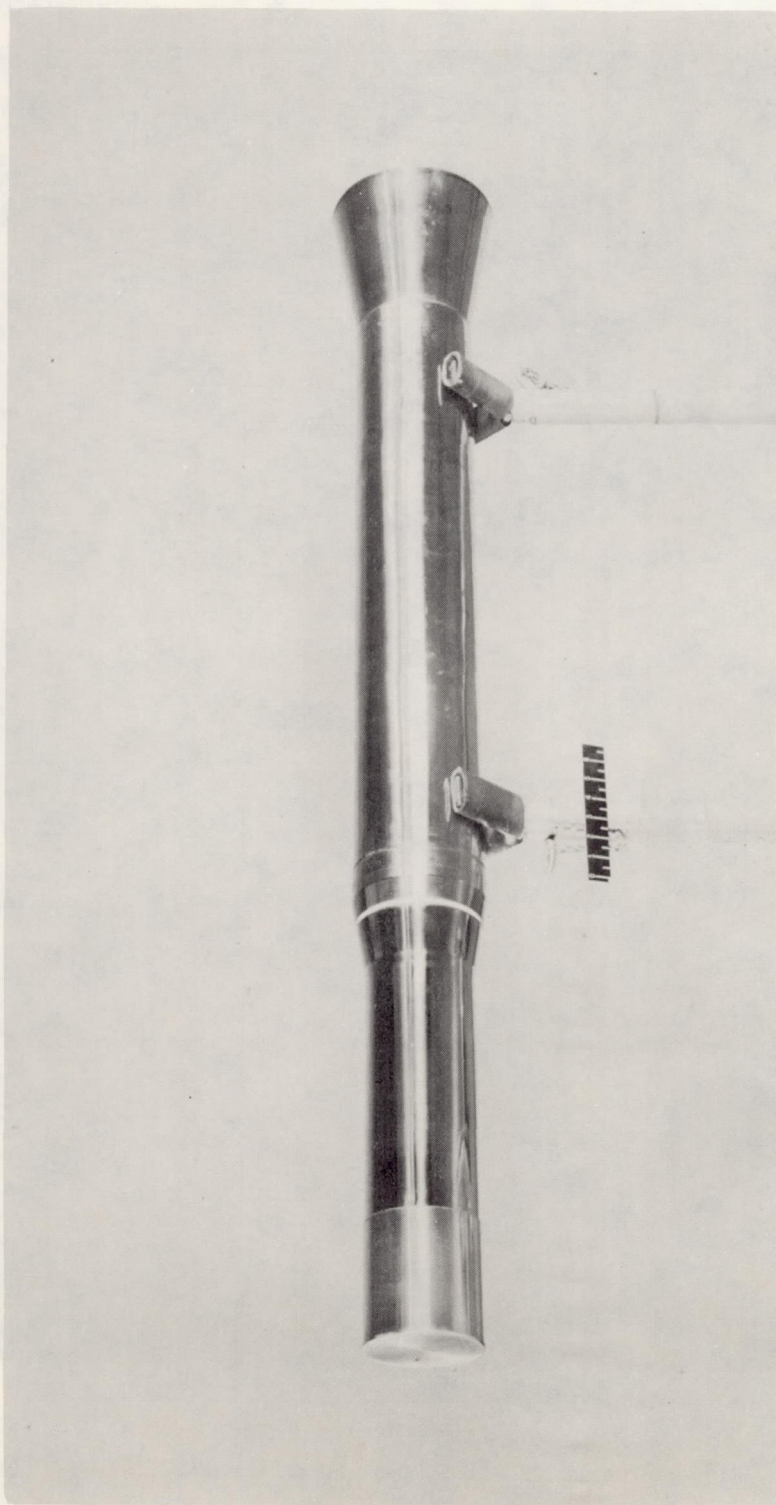
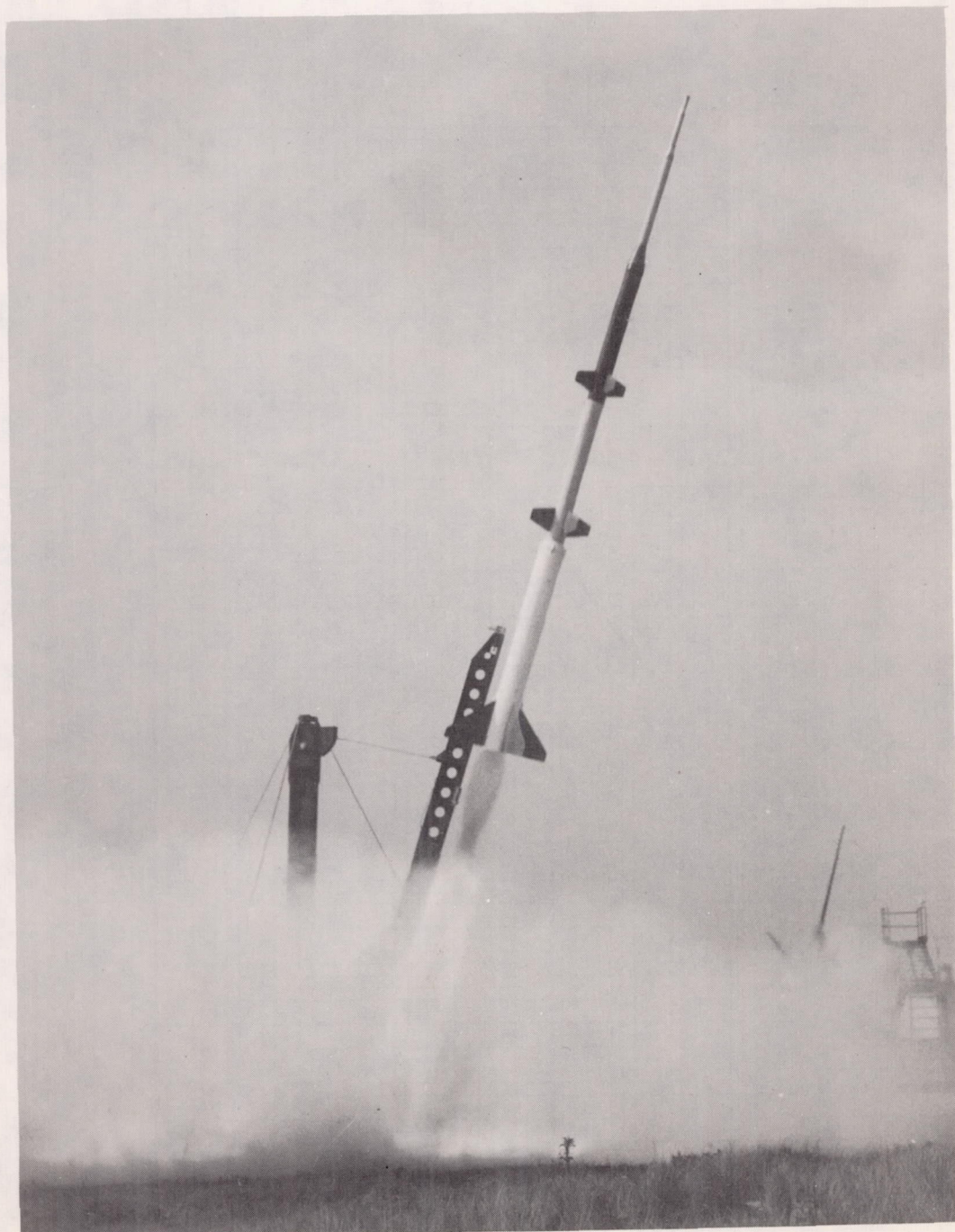


Figure 4.-- Photograph of model (fifth stage). L-57-2393



L-57-2802

Figure 5.- Photograph of model and four booster stages leaving the launcher.

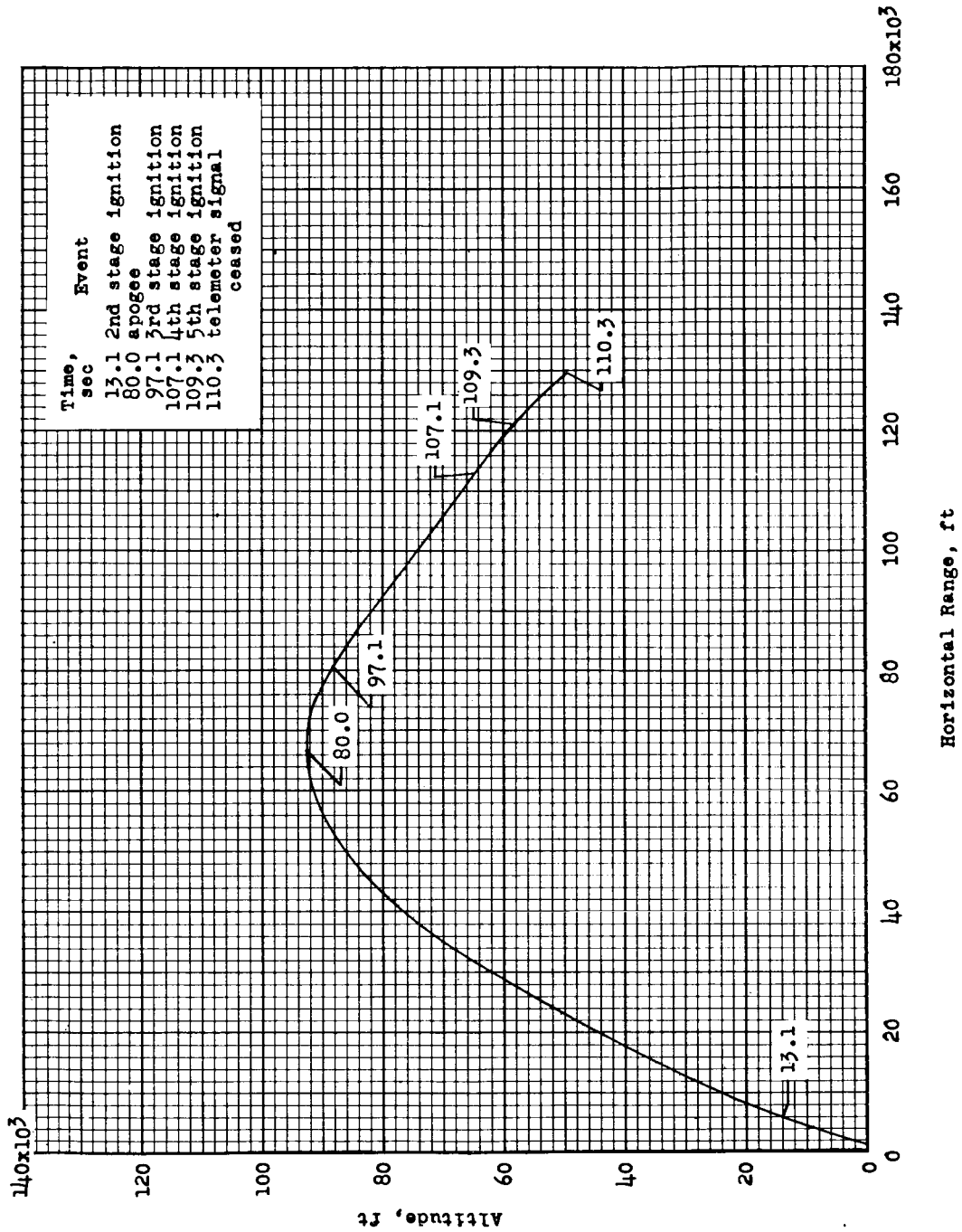
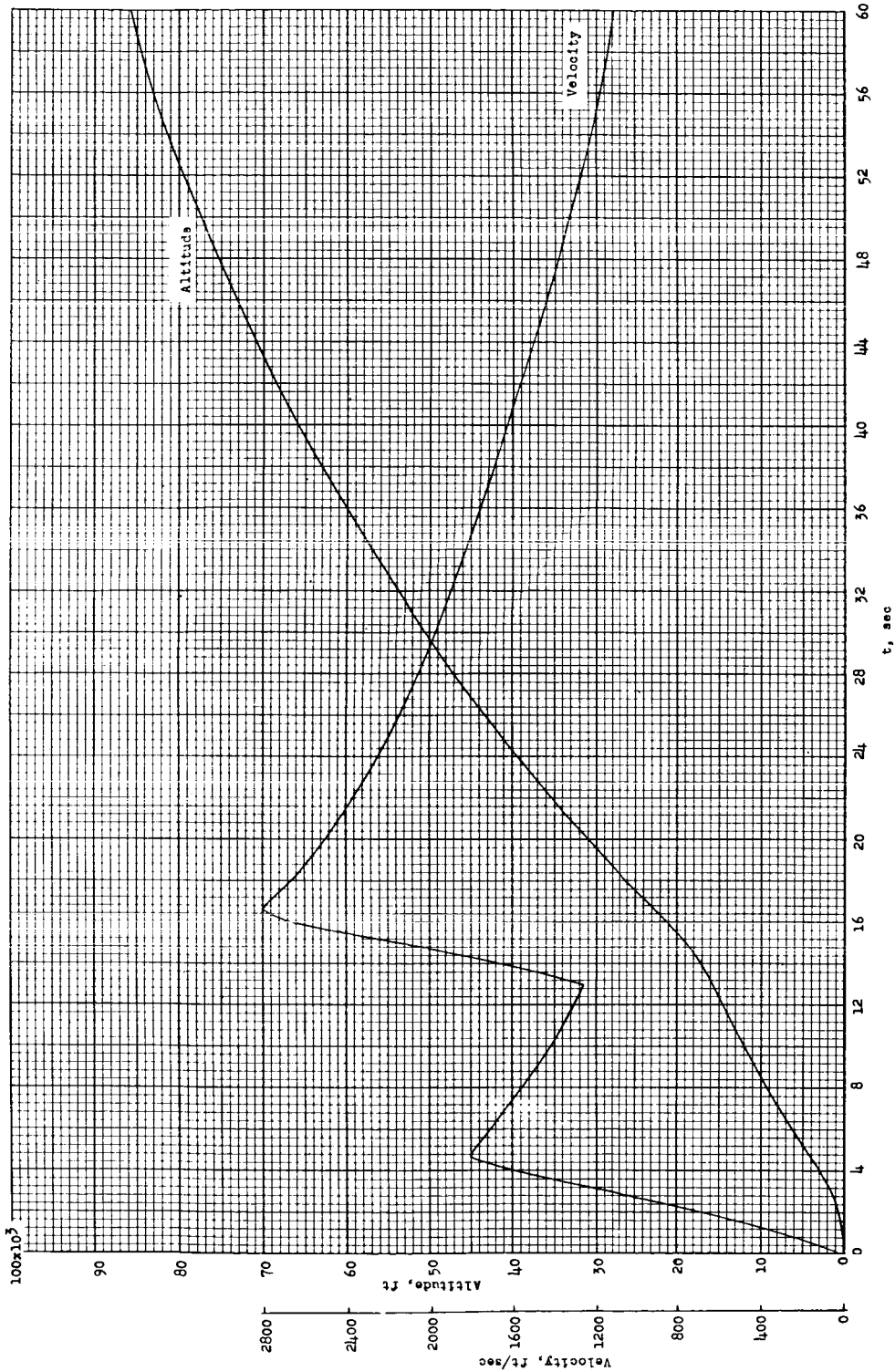
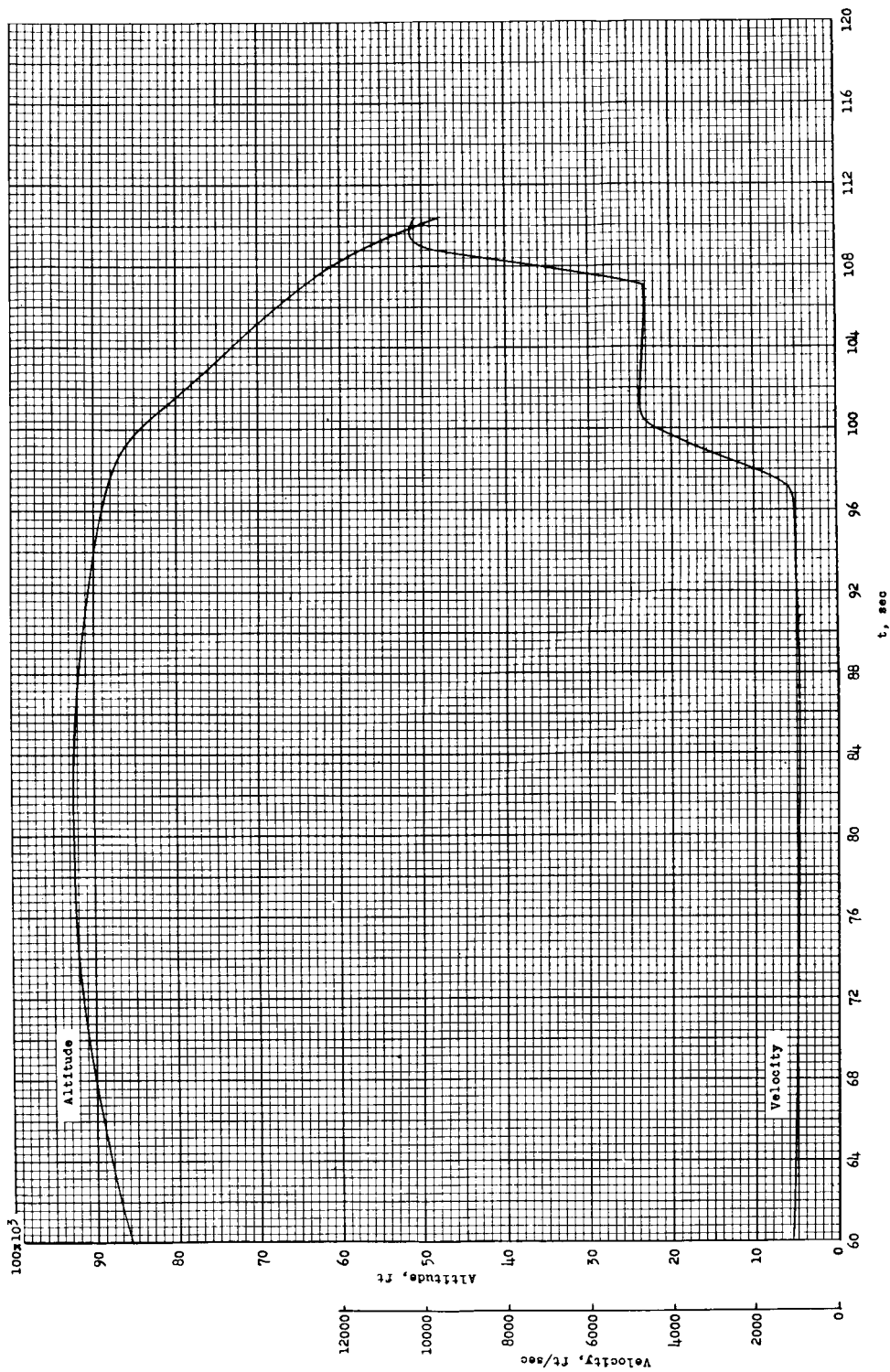


Figure 6.- Model trajectory to the time that the telemeter signal ceased.



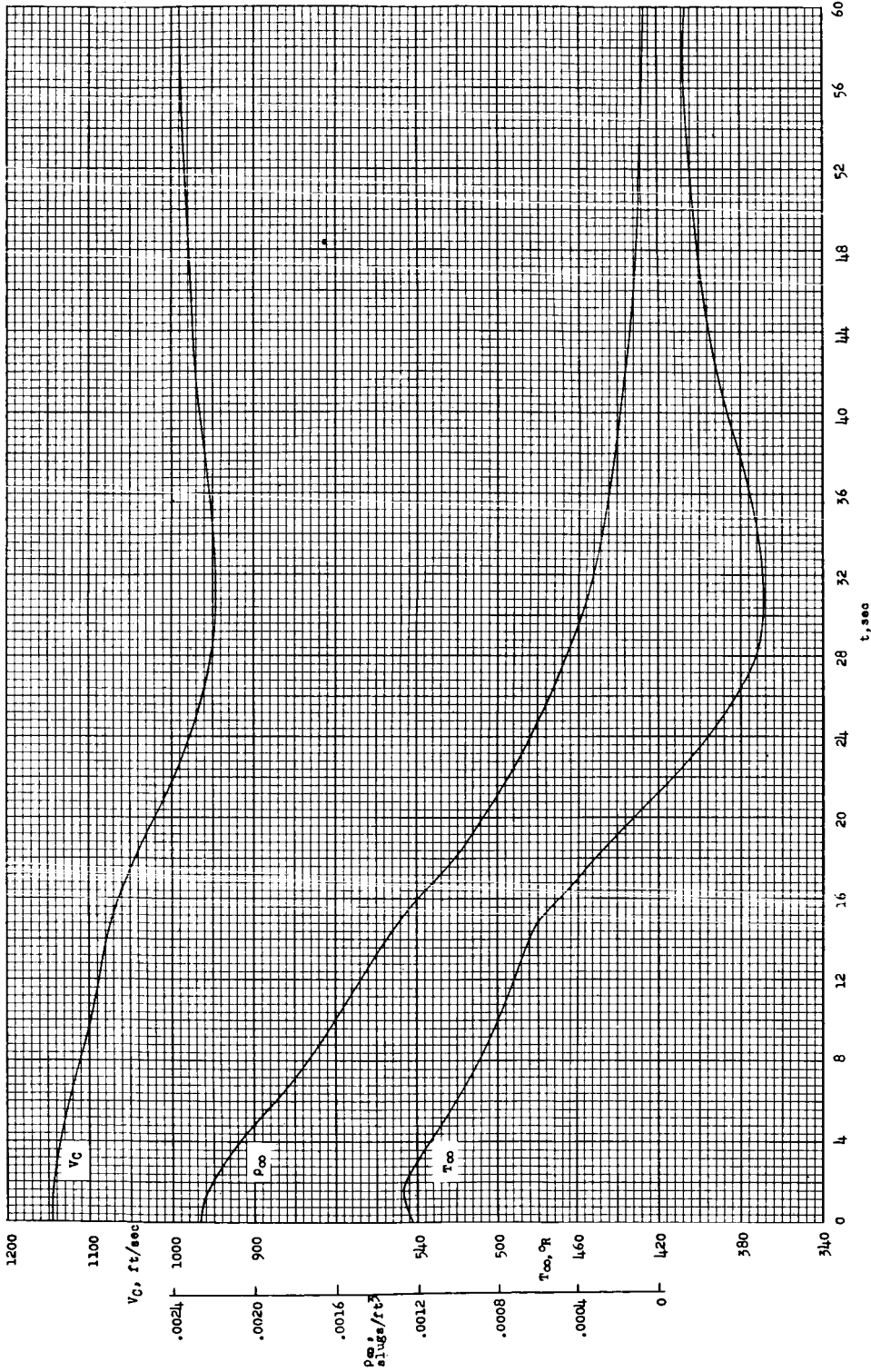
(a) 0 to 60 seconds.

Figure 7.- Time histories of altitude and free-stream velocity.



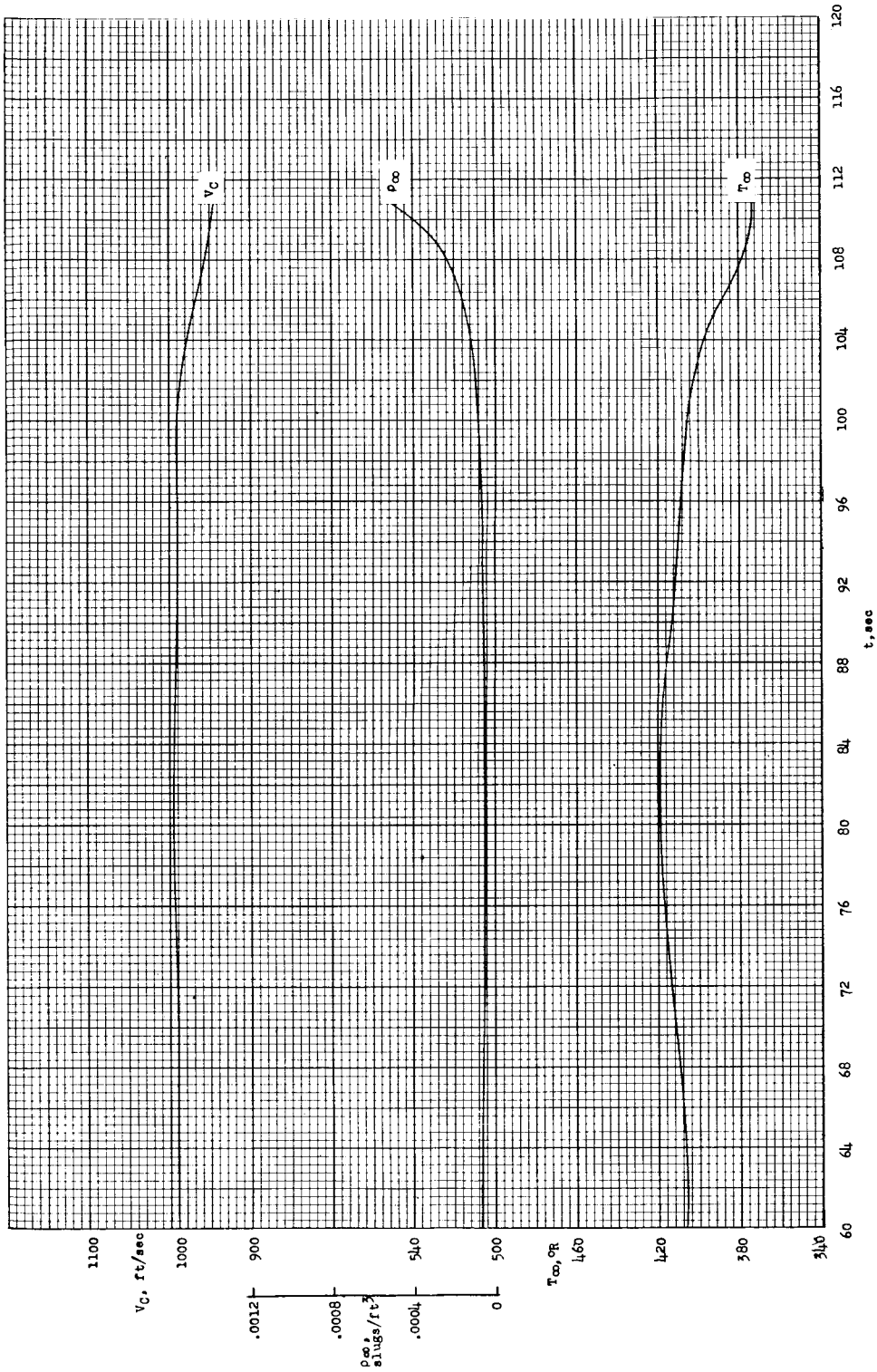
(b) 60 to 120 seconds.

Figure 7.- Concluded.



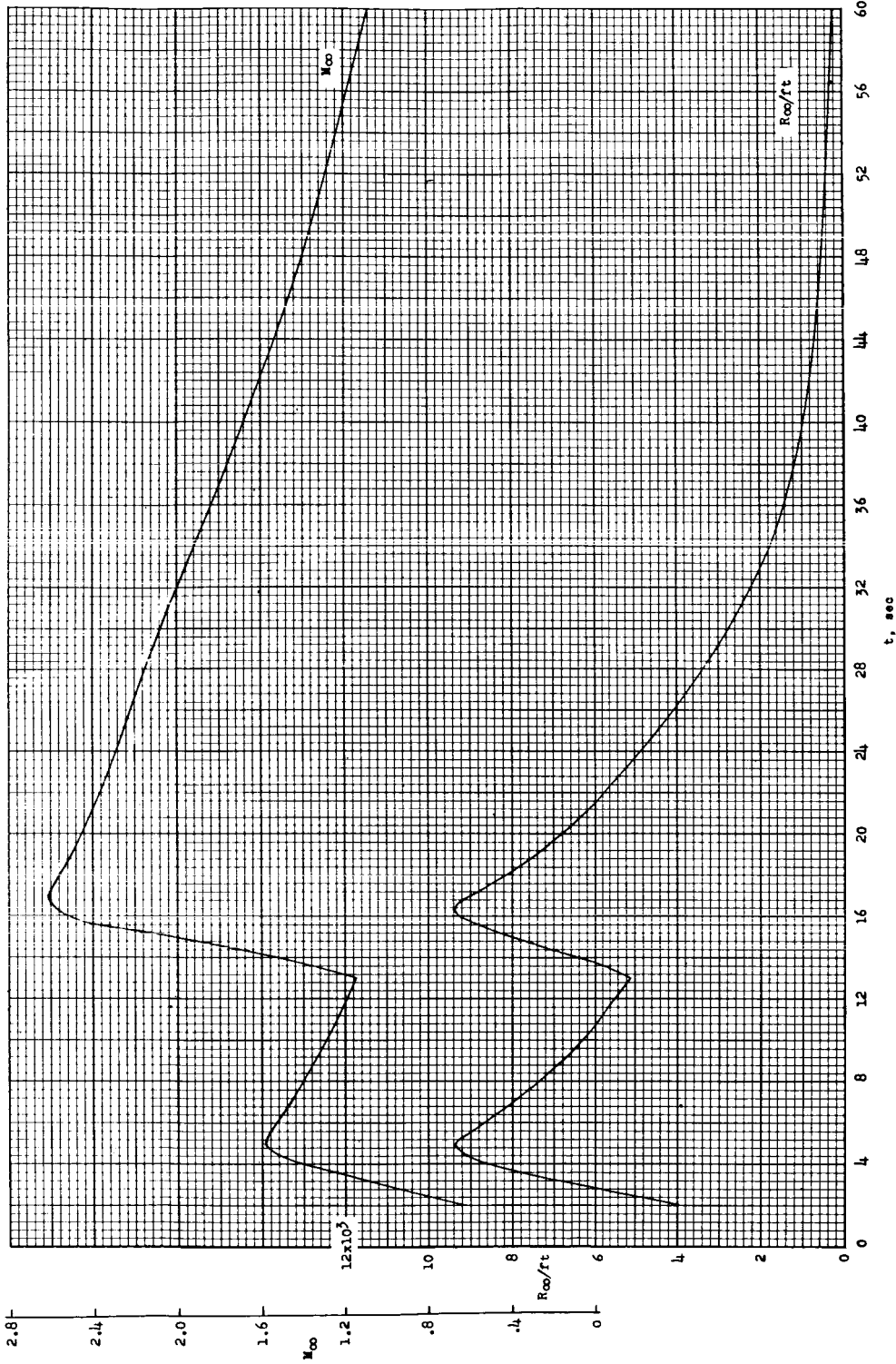
(a) 0 to 60 seconds.

Figure 8.- Time histories of atmospheric density, temperature, and velocity of sound.



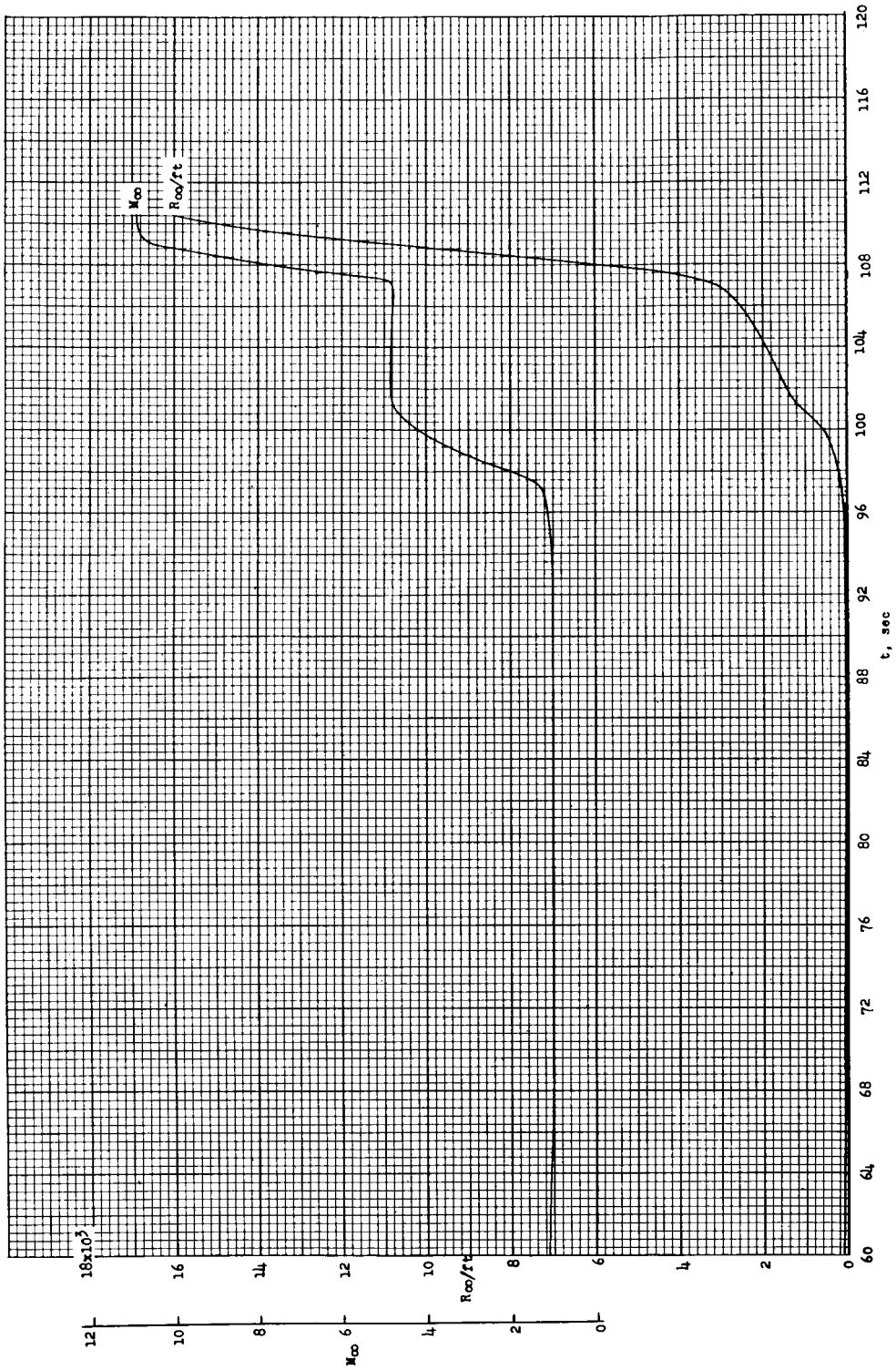
(b) 60 to 120 seconds.

Figure 8.- Concluded.



(a) 0 to 60 seconds.

Figure 9.- Time histories of free-stream Mach number and Reynolds number per foot.



(b) 60 to 120 seconds.

Figure 9.- Concluded.

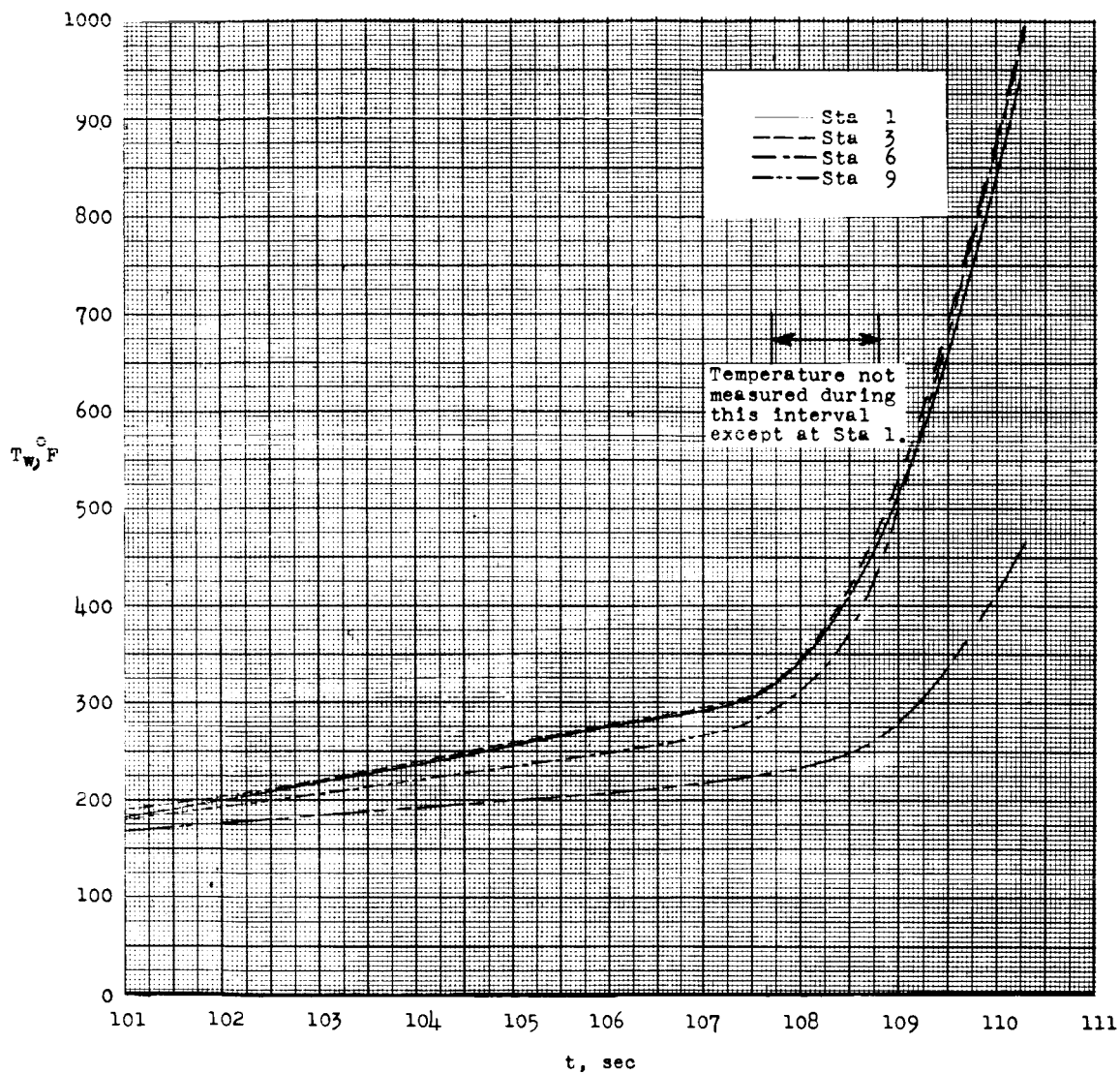


Figure 10.- Variation of measured inside wall temperatures at several stations on the nose.

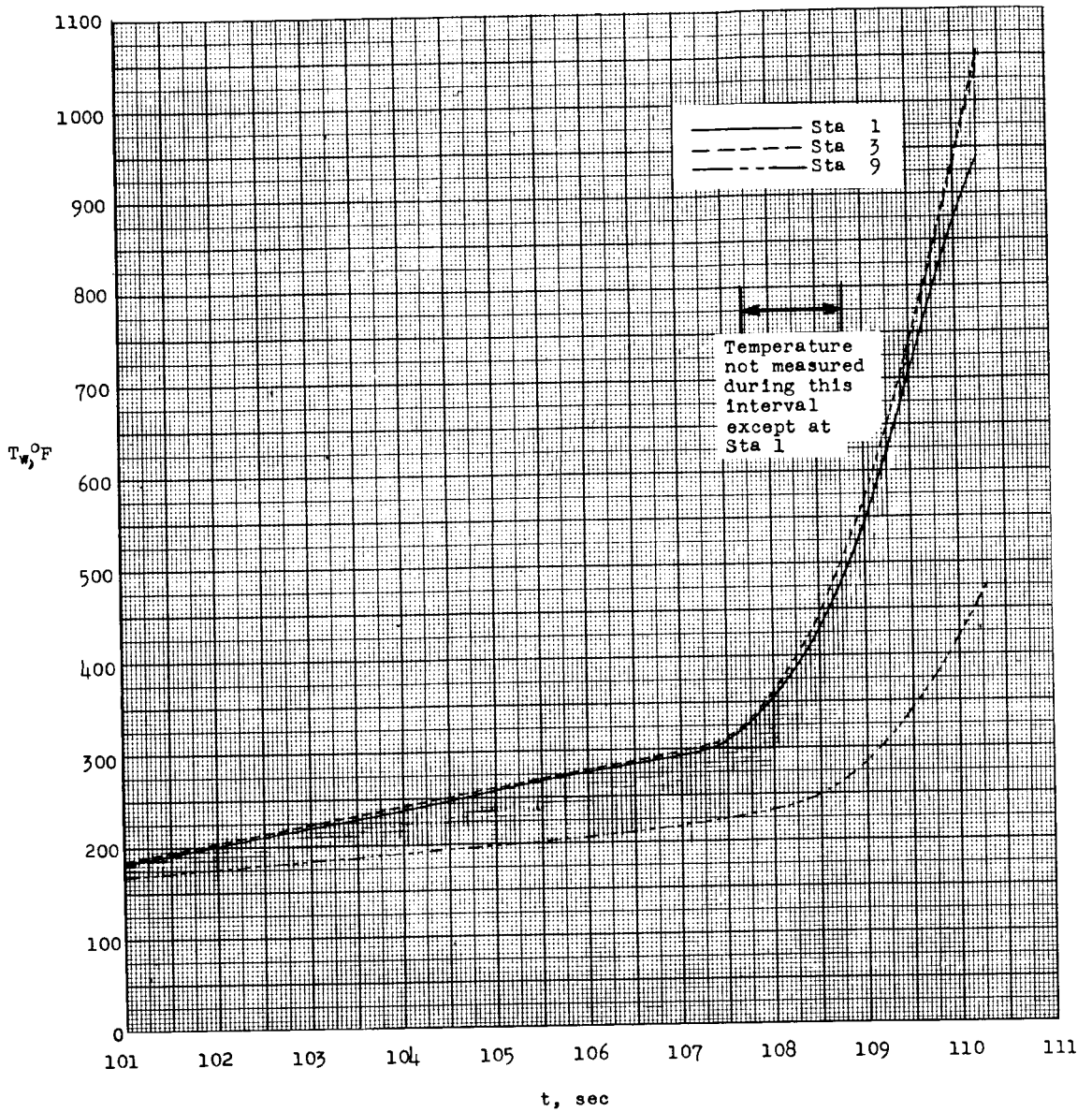
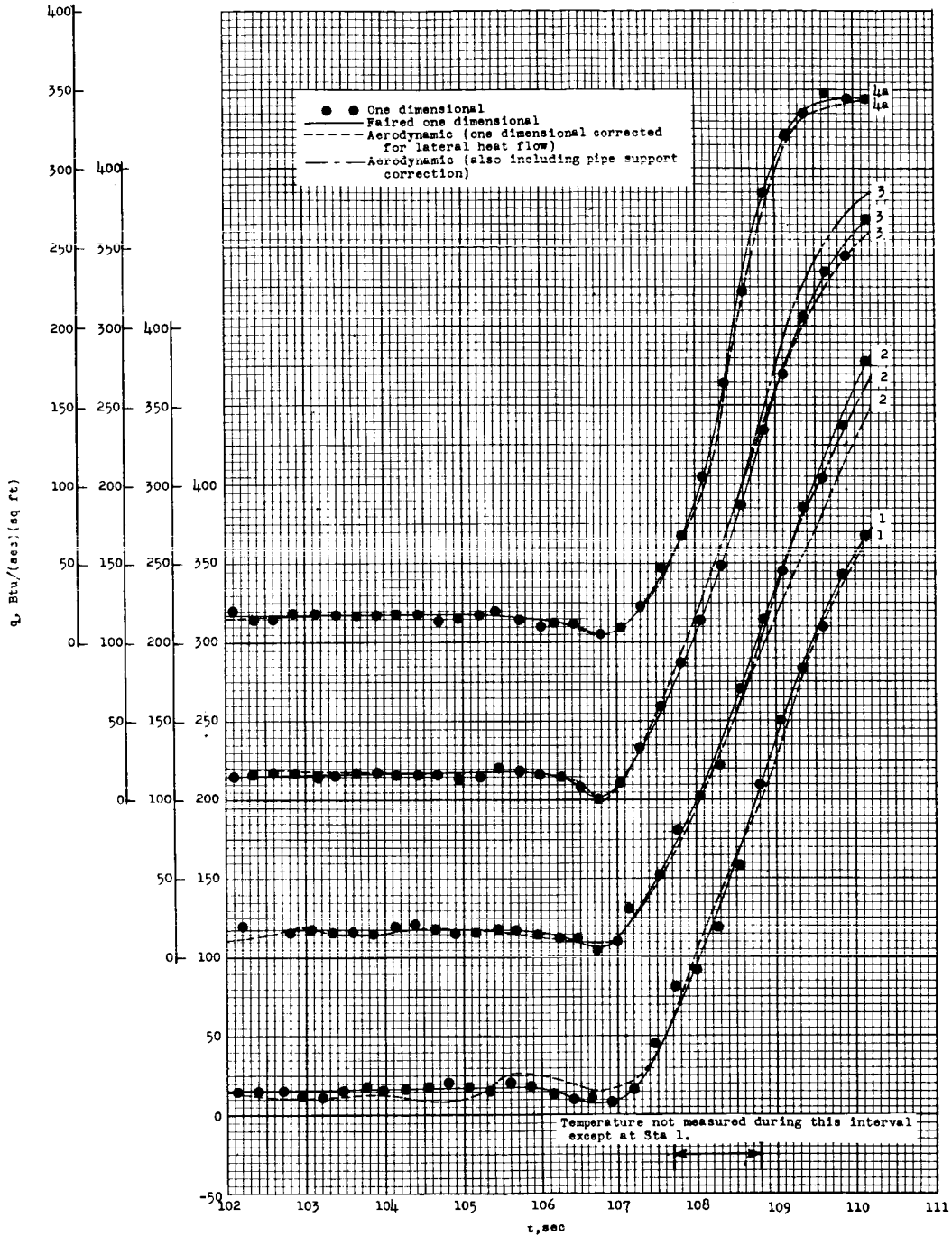
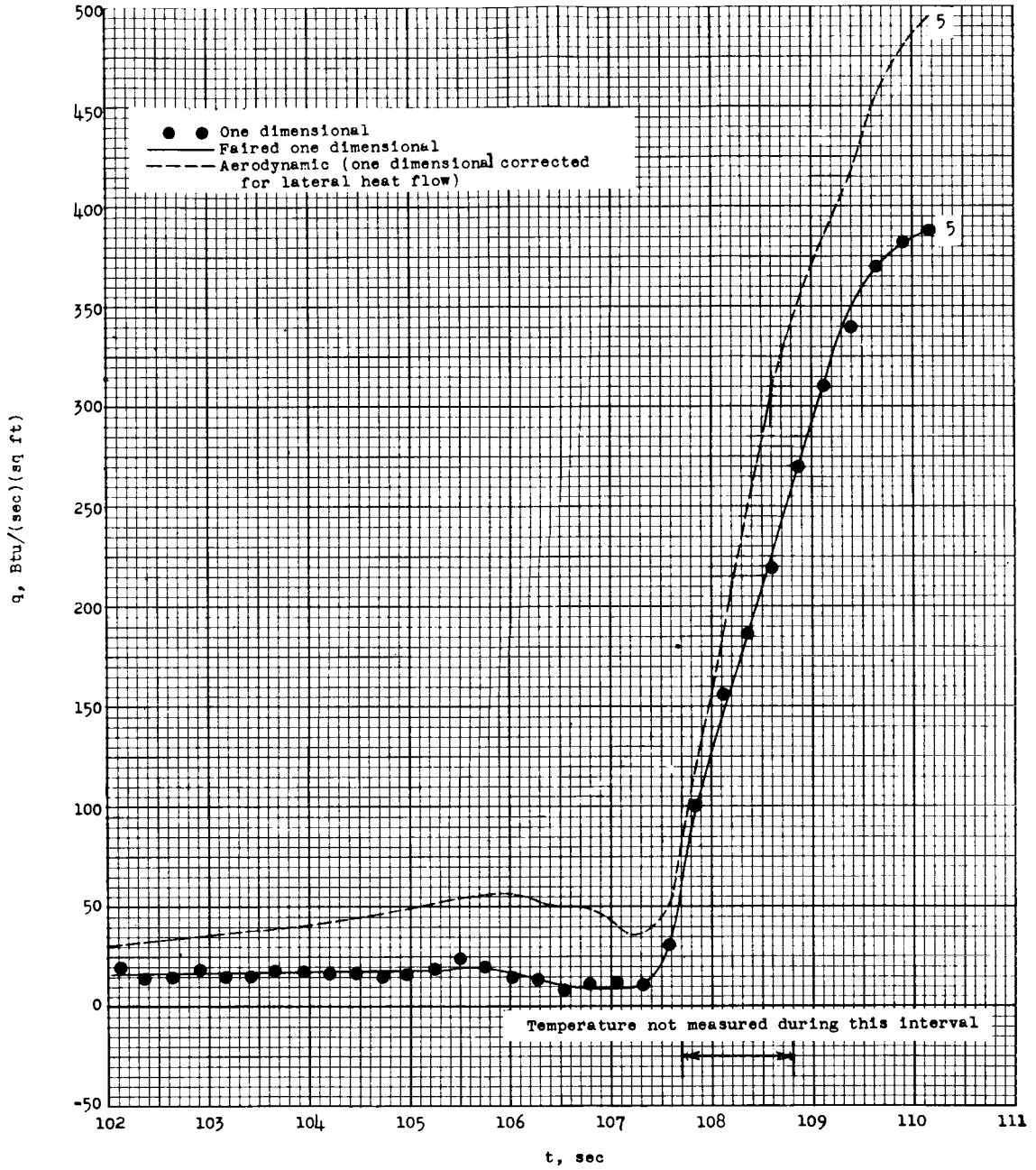


Figure 11.- Variation of calculated outside wall temperature at several stations on the nose.



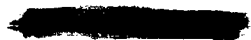
(a) Temperature measuring stations 1 to 4a.

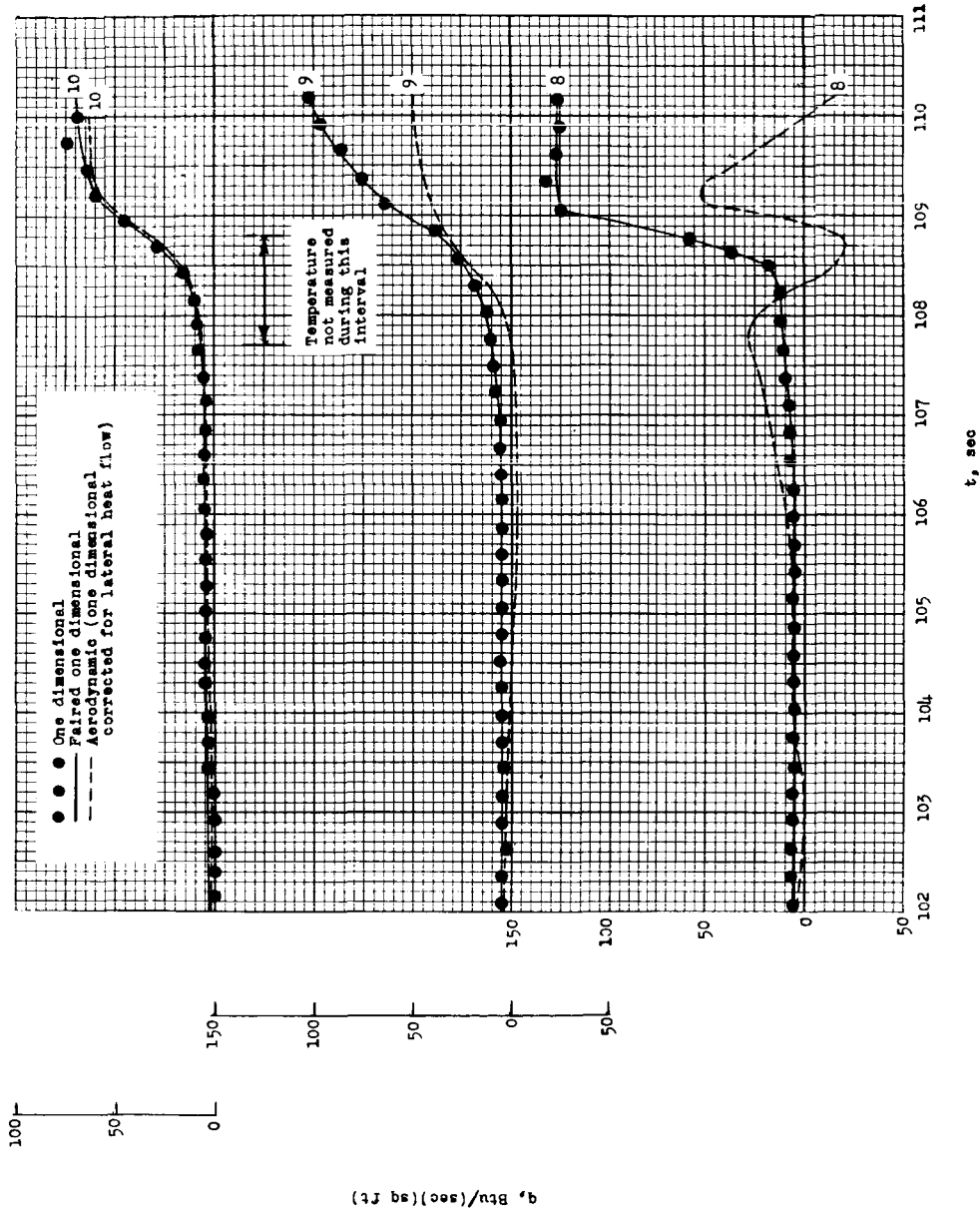
Figure 12.- Variation of heating rates with time.



(b) Temperature measuring station 5.

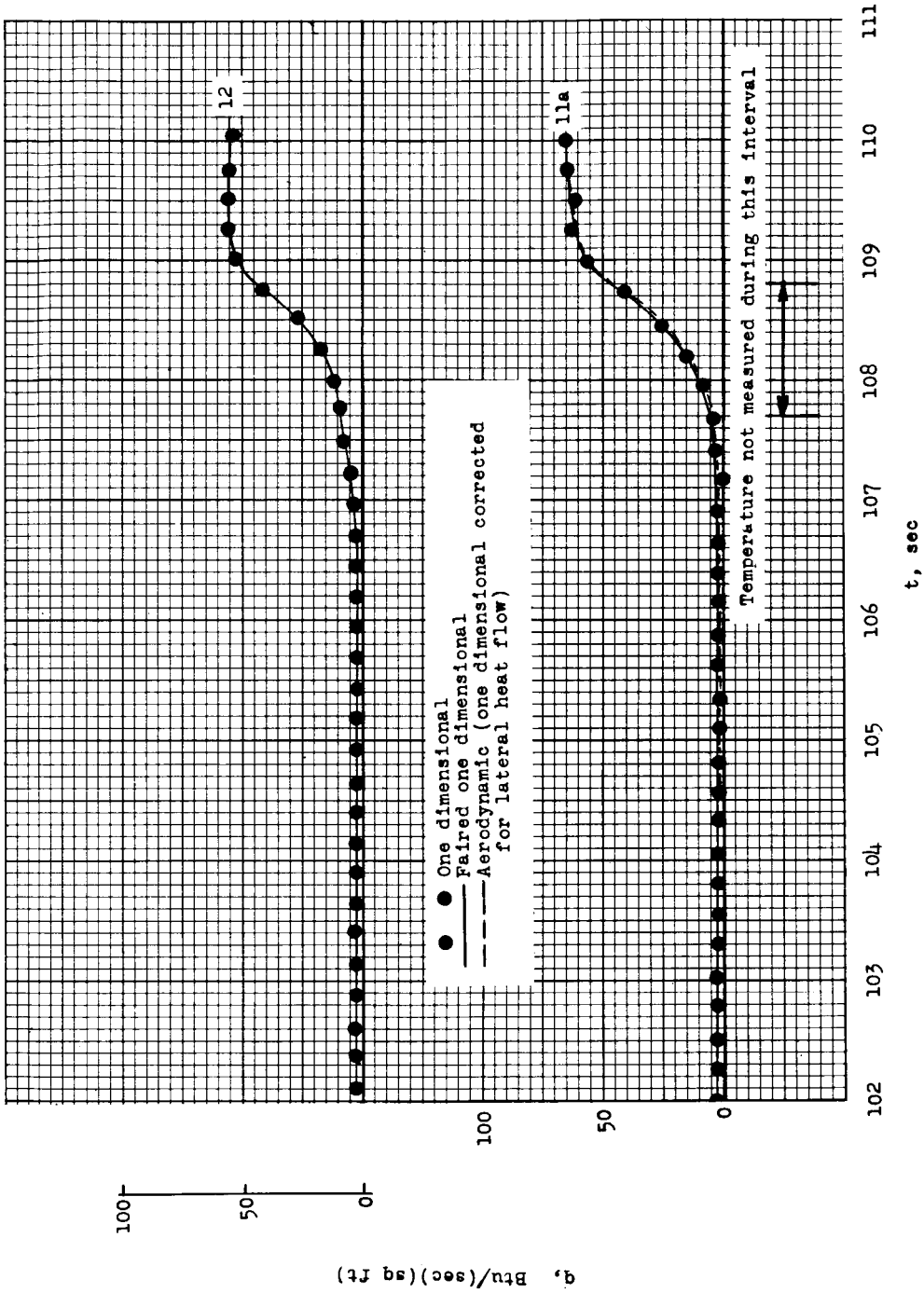
Figure 12.- Continued.





(c) Temperature measuring stations 8 to 10.

Figure 12.- Continued.



(d) Temperature measuring stations 11a and 12.

Figure 12.- Concluded.

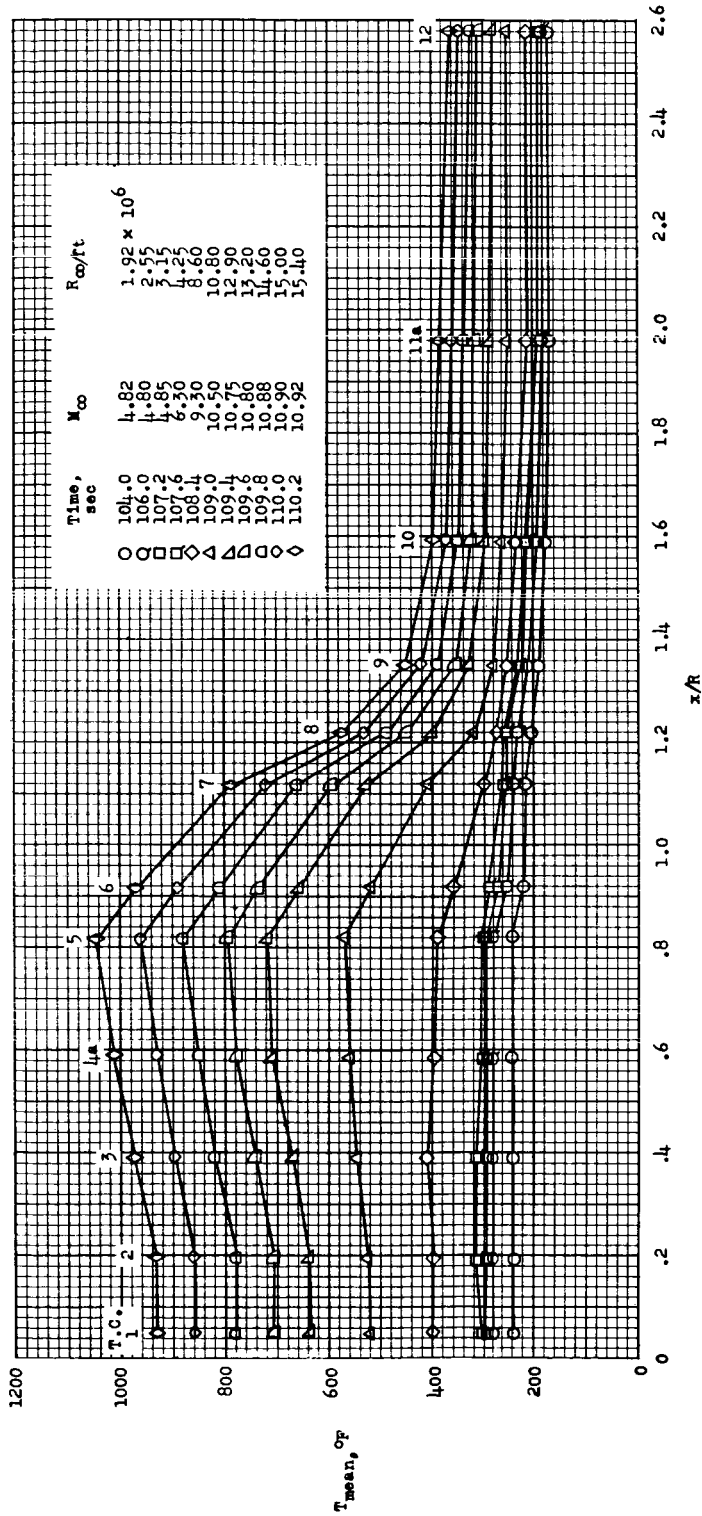


Figure 13.- Distribution of mean wall temperature in the nose at selected times.

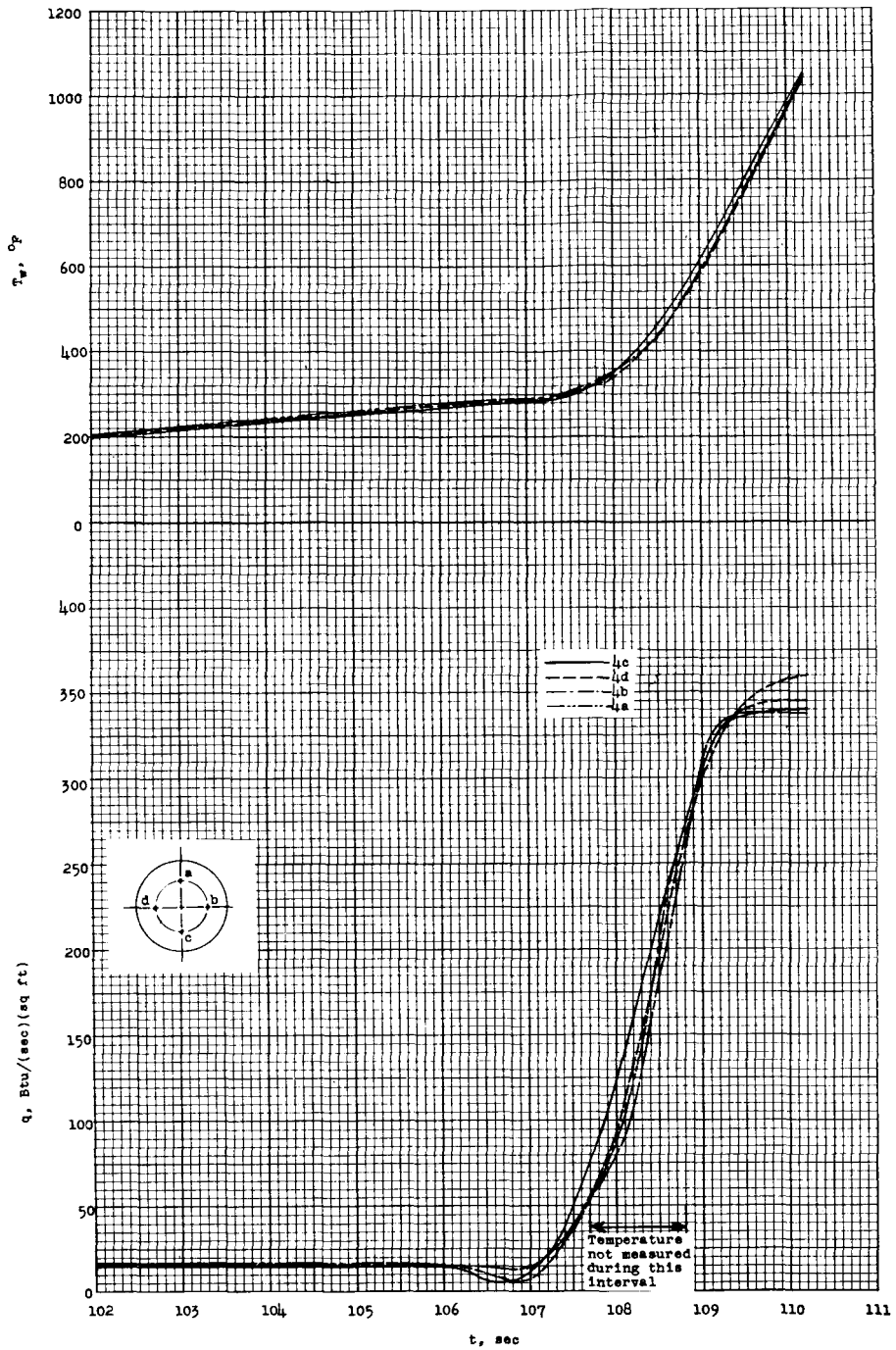


Figure 14.- Variation of measured temperature and one-dimensional heating rates with time at four locations on the flat nose equidistance from the center.

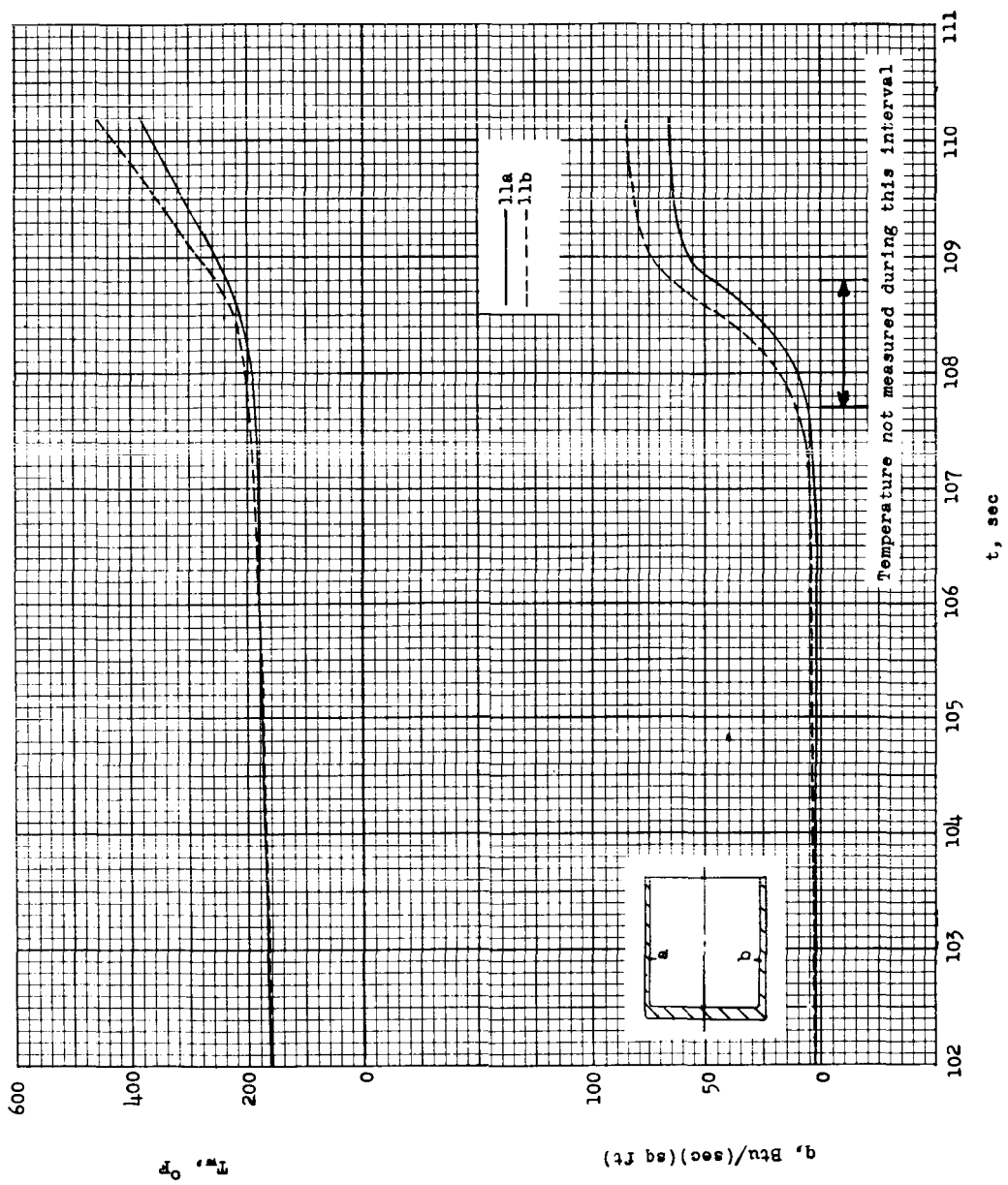


Figure 15.- Variation of measured temperatures and one-dimensional heating rates with time at two locations on the cylinder equidistant from the center of the flat nose.

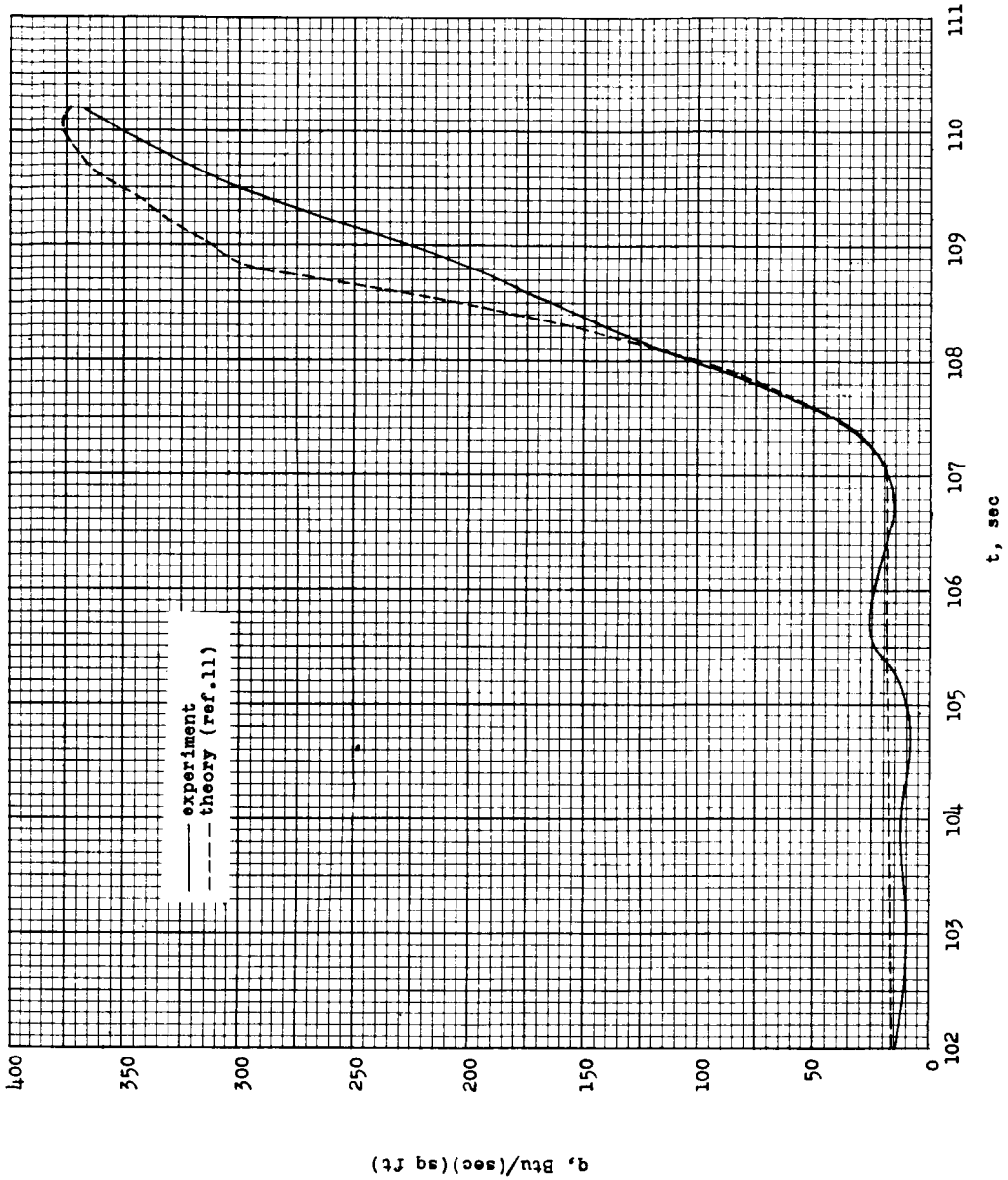
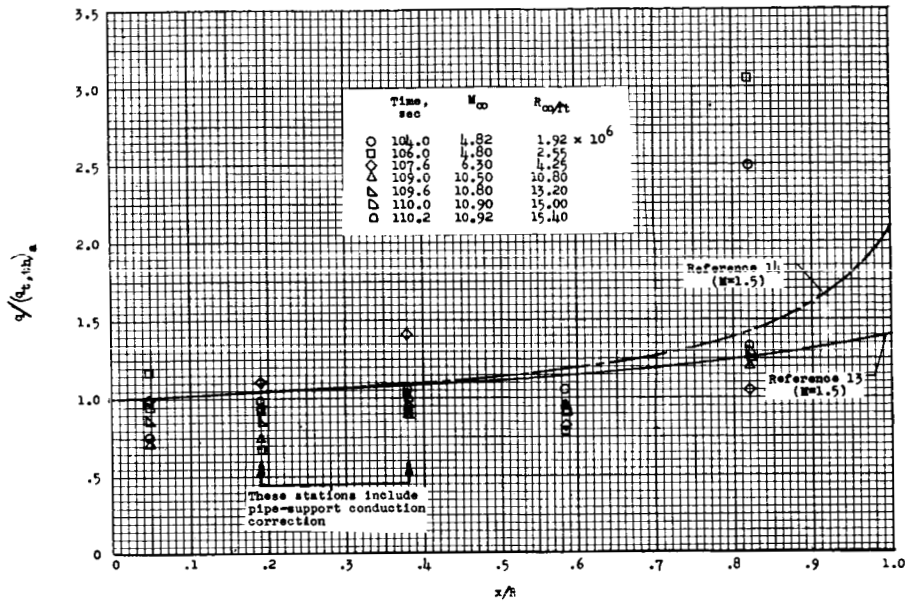
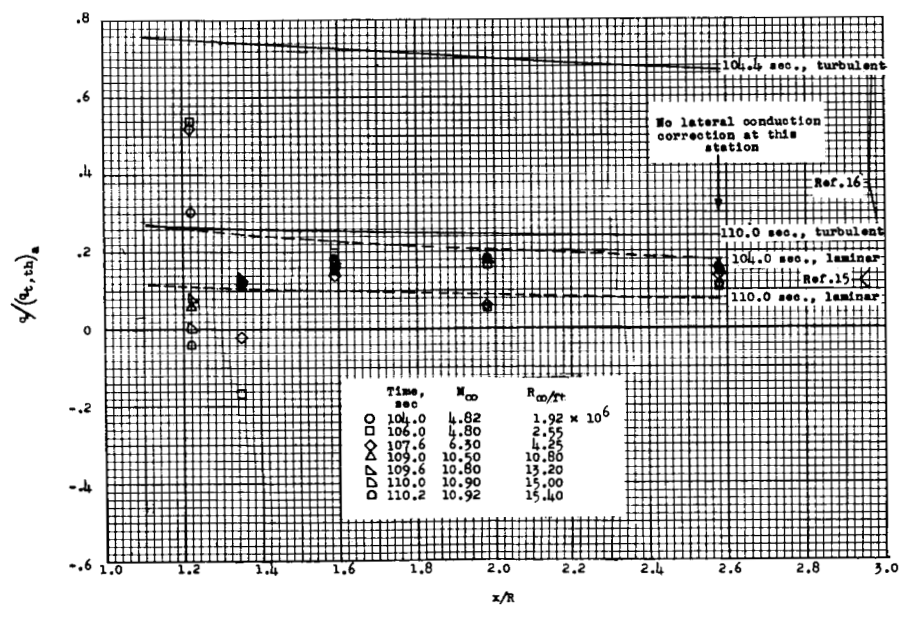


Figure 16.- Comparison of measured and theoretical aerodynamic-heating rates at the center of the flat nose (nominal stagnation point).

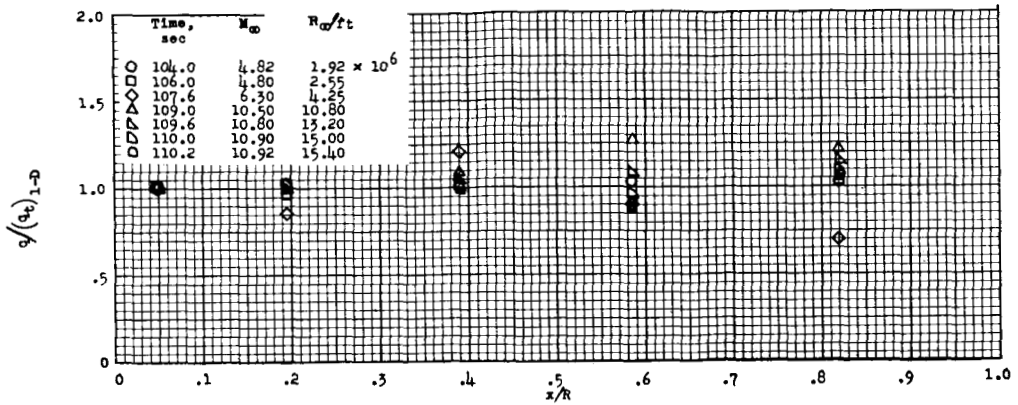


(a) Flat nose.

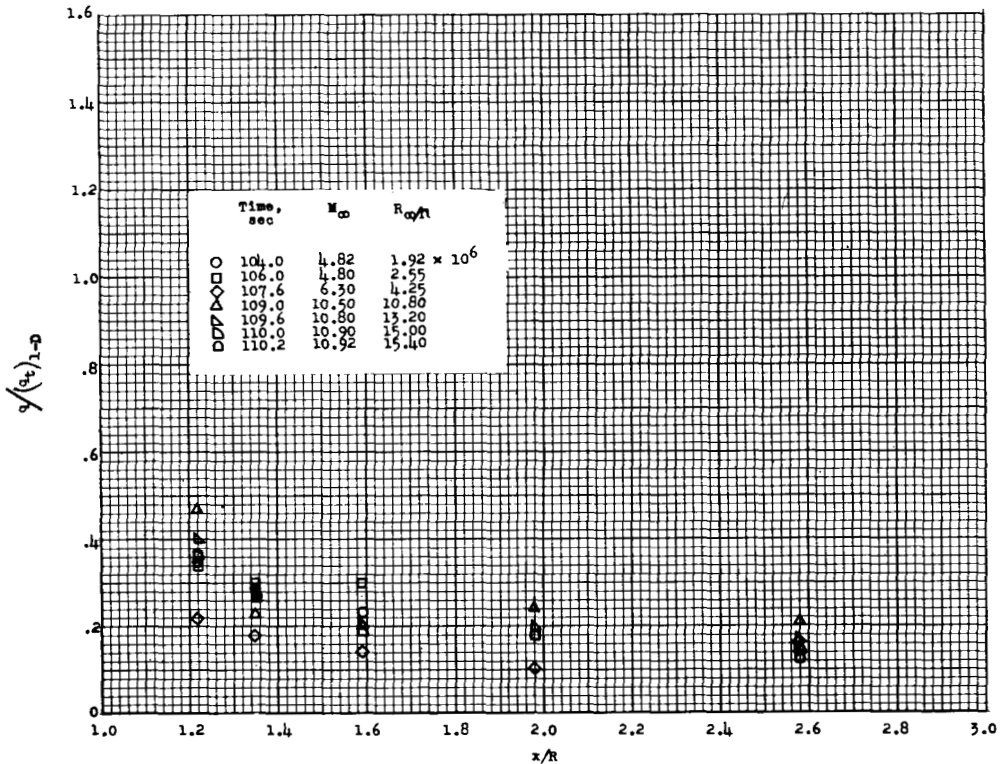


(b) Cylinder.

Figure 17.- Comparison of ratio of local measured and theoretical aerodynamic-heating rates to theoretical stagnation-point heating rates.



(a) Flat nose.



(b) Cylinder.

Figure 18.- Distribution over the nose of measured heating rates (with only one-dimensional heat flow considered) as ratios of local rates to rates at station 1.